Hybrid Metal-Phenol Nanoparticles with Polydopamine-like Coating for PET/SPECT/CT Imaging

Salvio Suárez-García[a], Tullio V. F. Esposito[b,c], Jenna Neufeld-Peters[b], Marta Bergamo[b,c], Hua Yang[d], Katayoun Saatchi[b], Paul Schaffer[d], Urs O. Häfeli[b,c], Daniel Ruiz-Molina[a,]*, Cristina Rodríguez-Rodríguez[b,e,]*, and Fernando Novio [a,f]*

[a]Catalan Institute of Nanoscience and Nanotechnology (ICN2), CSIC and BIST, Campus UAB, Bellaterra, 08193 Barcelona, Spain.

[b]Faculty of Pharmaceutical Sciences, University of British Columbia, Vancouver, BC V6T 1Z3, Canada.

[c]Department of Pharmacy, Faculty of Health and Medical Sciences, University of Copenhagen, 2100 Copenhagen, Denmark.

[d]TRIUMF, 4004 Wesbrook Mall, Vancouver, BC V6T 2A3, Canada.

[e]Department of Physics and Astronomy, University of British Columbia, Vancouver, BC V6T 1Z1, Canada.

[f]Departament de Química, Universitat Autònoma de Barcelona (UAB), Campus UAB, Cerdanyola del Vallès 08193, Barcelona, Spain

*Dr. Daniel Ruiz-Molina. Ph: +(34) 93733614. *E-mail*: dani.ruiz@icn2.cat

*Dr. Cristina Rodríguez-Rodríguez. Ph: +(01) 604.827.1833. *E-mail*: cristina.rodriguez@ubc.ca

*Dr. Fernando Novio. Ph: +(34) 937372648. *E-mail*: fernando.novio@icn2.cat

KEYWORDS: *Nanoscale Coordination Polymers, Metal-Phenol Nanoparticles, Polydopamine-Like Coating, Radioimaging, SPECT/PET, ^{111}In-labeling, ^{64}Cu-labeling*

ABSTRACT

The validation of metal-phenolic nanoparticles (MPNs) in preclinical imaging studies represents a growing field of interest due to their versatility in forming predesigned structures with unique properties. Before MPNs can be used in medicine, their pharmacokinetics must be optimized so that accumulation in non-targeted organs is prevented and toxicity minimized. Here, we report the fabrication of MPNs made of a coordination polymer core that combines In(III), Cu(II) and a mixture of the imidazole 1,4-bis(imidazole-1-ylmethyl)-benzene and the catechol 3,4-dihydroxycinnamic acid ligands. Furthermore, a phenolic-based coating was performed used as an anchoring platform to attach polyethylene glycol (PEG). The resulting MPNs, with effective hydrodynamic diameters of around 120 nm, could be further derivatized with surface embedded molecules, such as folic acid, to facilitate *in vivo* targeting and multifunctionality. The prepared MPNs were evaluated for *in vitro* plasma stability, cytotoxicity and cell internalization and found to be biocompatible under physiological conditions. First biomedical evaluations were then performed by intrinsically incorporating trace amounts of the radioactive metals ^{111}In or ^{64}Cu during the MPN synthesis directly into their crystal lattice. The resulting particles, which had identical physicochemical properties to their non-radioactive counterparts, were used to perform *in vivo* single-photon emission computed tomography (SPECT) and positron emission tomography (PET) in tumor-bearing mice. The ability to incorporate multiple metals and radiometals into MPNs illustrates the diverse range of functional nanoparticles that can be prepared with this approach and broadens the scope of these nanoconstructs as multimodal preclinical imaging agents.

1. INTRODUCTION

(Poly)phenols are ubiquitous reactive metabolites abundant in nature. Their beneficial effects are, among others, antioxidant capacity, adhesive properties and metal-binding coordination, which have inspired the design and synthesis of numerous materials with applications in catalysis, biomedicine and theranostics.[1,2,3] Representative examples are metal-phenolic nanoparticles (MPNs), consisting of metal ions linked by polyphenol[4,5,6,7] or catechol ligands assisted by additional polymerizing bridging ligands via the self-assembly process.[8,9] These nanoparticles (NPs) have shown excellent coordination capabilities combined with good biocompatibility, biodegradation, antioxidant capacities and have an accessible surface for modification.[10,11,12,13] Furthermore, as recently reviewed by Caruso et al.[14], the broad range of metal ions used to prepare these NPs provides a unique multifunctional character to these NPs that can be exploited for biomedical applications, such as drug delivery and imaging. Several MPNs based on Fe, Cu, Pt and many others,[15] have shown encouraging results in preclinical biomedical imaging applications,[16] especially in magnetic resonance imaging (MRI).[17,18,19] Nuclear imaging with MPNs, either positron emission tomography (PET) or single-photon positron tomography (SPECT), has been less explored.[20,21] At the time of writing this report, only a few examples of MPNs labeled with radionuclides exist. Examples include ^{89}Zr-based MPNs to assess particle uptake into tumors[22] and to monitor the delivery of carbonyl reductase inhibitors[23] or platinum prodrugs into tumors with MPN-based drug delivery systems.[24,25] ^{64}Cu has also been incorporated into the matrix of MPNs for tumor uptake studies,[26,27] and related pharmacokinetic evaluations.[15] A common feature of the radiolabeled MPNs to date has been a rapid and significant uptake into the reticuloendothelial system (RES), namely the liver and spleen, following intravenous (i.v.) injection. Tumor uptake with these radiolabeled MPNs has been marginal in most studies, likely due to RES sequestration. Altering the pharmacokinetics of radiolabeled MPNs, such as their blood-circulating and targeting properties, is crucial to improving the safety and efficacy profile of this promising NP class and to advance MPNs into high-value applications; to do so, however, will require mastering of MPN surface modification and functionalization, which is no small feat.

Beyond crosslinking with metal ions, the covalent polymerization of phenols such as dopamine,[28,29] L-3,4-dihydroxyphenylalanine (L-DOPA)/norepinephrine,[30,31,32,33] or other catechol/galloyl groups[34] mimicking the astonishing adhesive properties of mussel-segregated polymers has also been broadly followed.[29,35] In addition to nanocapsules[36,37,38] and NPs,[39] the seminal breakthrough reported by Messersmith and co-workers in the synthesis of polydopamine (PDA)-based biocoatings[40] has led to broad acceptance of PDA as coatings over the years.[41] Therefore, PDA and related coating materials represent an impressive new approach in the area of nanomaterials and their interaction with biological environments. Especially relevant for this work is the decoration of NPs with PDA-like coating, which serves as an anchoring platform for the conjugation of polyethylene glycol (PEG) to impart improved colloidal stability in physiological media and *in vivo*.[42] .[43] NP surfaces can further be modified with ligands to actively target MPNs to specific tissues. Examples include the conjugation

of folic acid (FA) to the coating of NPs and other therapeutic ensembles to improve their accumulation in FA-receptor-positive tumors.[44,45] The addition of a PDA-like coating, PEG and a targeting moiety, such as FA, may represent another step in the optimization and biocompatibility of MPNs. To the best of our knowledge, no such hybrid MPNs have been described in the literature, and only Chen *et al.* reported seminal work with PDA-PEG coated MPNs labeled with [89]Zr.[46]

In this work, we present a simple one-step assembly method to synthesize MPNs by mixing In(III) with the imidazole **L1**, 1,4-bis(imidazole-1-ylmethyl)-benzene, and the catechol **L2**, 3,4-dihydroxycinnamic acid, as co-ligands.[47] The surface was then functionalized with a PDA-like coating by crosslinking pyrocatechol with hexamethylenediamine under oxidizing conditions,[48] a one-step method for the functional modification of nanomaterials,[49,50,51,52,53] followed by PEGylation and functionalization with FA. A radioactive version of these MPNs was prepared chelator free by mixing in [111]In(III) during the initial synthesis. With a relatively long half-life of 2.807 days, the ^{111}In-labeled MPNs were used for *in vitro* assessments, such as stability and cell uptake studies, and for preclinical SPECT/CT imaging. To assess whether the addition of FA moieties targeted the MPNs *in vivo*, the distribution of radiolabeled **In-MPN-FA** was compared to **In-MPN-PEG** in mice bearing CT26 tumors that overexpress FA-receptors. Finally, the ability of the synthesized MPNs to simultaneously incorporate metal ions, motivated us to further radiolabel homologous **Cu-MPN-PEG** NPs with [64]Cu(II), a positron emitter with a half-life of 12.7 h, and to evaluate the resulting MPN's suitability for diagnostic PET imaging. A schematic representation of the whole synthetic process is shown in **Figure 1**.
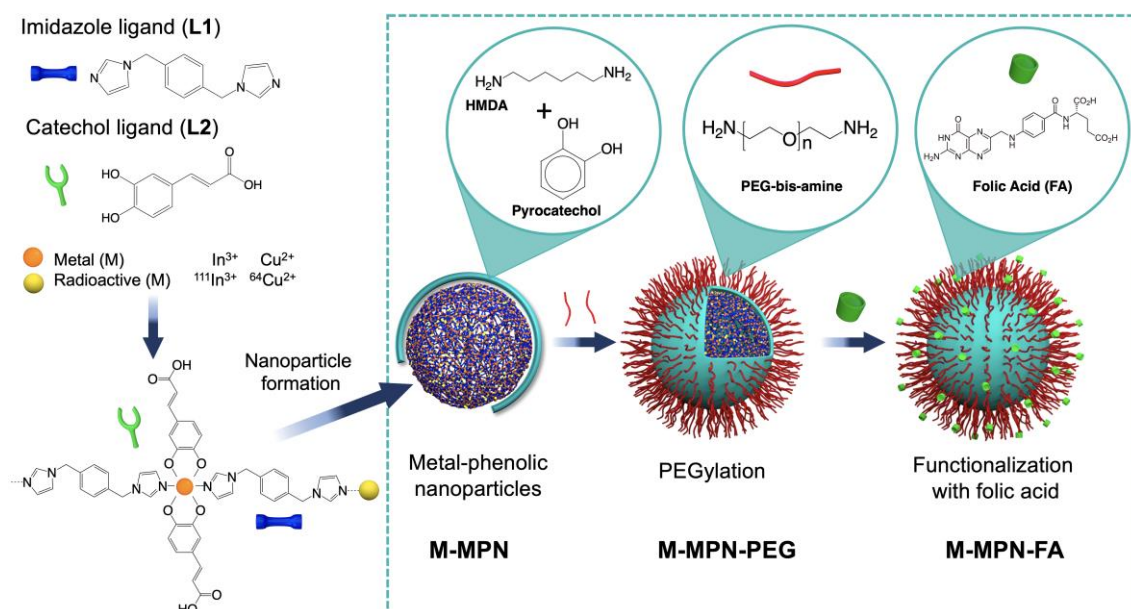
Figure 1. Schematic procedure for the formation of multifunctional metal-phenolic nanoparticles (MPNs) for preclinical targeted imaging. The MPNs were synthesized by combining the metals indium In(III) or copper Cu(II) and their corresponding radioisotopes ^{111}In or ^{64}Cu with imidazole and catechol-based organic ligands. The formed MPNs were coated with a universal phenol-based platform used for the anchoring of polyethylene glycol (PEG) molecules and folic acid (FA) moieties.

2. EXPERIMENTAL SECTION

2.1 Materials. Indium chloride and copper chloride (Sigma-Aldrich, Merck, Madrid, Spain) were used for chelation together with ^{111}In provided as a ^{111}InCl$_3$ solution in 0.05 M HCl (BWTX, Vancouver, BC, Canada). The imidazole **L1**, 1,4-bis(imidazole-1-ylmethyl)benzene was synthesized according to a previously reported methodology.[54] The co-ligand catechol **L2**, 3,4-dihydroxycinnamic acid was purchased from Sigma-Aldrich. Solvents were used as received without additional drying or degassing (Scharlab, Madrid, Spain). All other reagents were obtained from Sigma-Aldrich or Merck unless otherwise specified. Type 1 ultrapure water from in-house Milli-Q filtration systems (Millipore, Burlington, MA, USA) was used in all experiments, unless otherwise specified.

2.2 ^{64}Cu production. ^{64}Cu was produced from enriched ^{64}Ni solid target at the TRIUMF TR13 cyclotron (Vancouver, BC, Canada). In brief, 50 mg isotopically enriched ^{64}Ni metal powder (Isoflex, San Francisco, CA, USA) was dissolved in HCl. Aqueous ammonia was added to adjust the pH to ~9. ^{64}Ni was then electroplated onto a rhodium backing disk (35 mm diameter, 1 mm thickness) using a small custom plating apparatus overnight. Subsequently, the disk was rinsed with water and dried at 110 °C in an oven. The plated nickel layer was approximately 8 mm in diameter and 110 μm thick. The target was irradiated for 1 h at 10 μA proton current and left in the cyclotron for 2 h to allow for the decay of the short-lived isotopes (**Table S15**). The ^{64}Ni layer of the target was dissolved in hot concentrated HCl, evaporated to dryness, the residue re-dissolved in 6 M HCl and loaded onto an AG1-X8 column (1 cm, pre-conditioned with 5 bed volumes of 6 M HCl). The column was washed with 10 mL 6 M HCl and ^{64}Cu eluted with water.

2.3 Synthesis of In-MPN and Cu-MPN. 1,4-Bis(imidazole-1-ylmethyl)-benzene (**L1** - 6 mg, 0.25 mmol) and 3,4-dihydroxycinnamic acid (**L2** - 9 mg, 0.5 mmol) were dissolved in 0.8 mL of ethanol. Subsequently, the solution was treated with an aqueous solution containing the metal salt InCl$_3$ (7.3 mg, 0.25 mmol in 2 mL H$_2$O) to obtain the non-radioactive **In-MPN** or together with ^{111}InCl$_3$ (94.35 ± 16.26 MBq, 2-5 μL in 0.05 M HCl) to obtain ^{111}**In-MPN**; or the metal salt CuCl$_2$ (5.2 mg, 0.25 mmol in 0.2 mL H$_2$O) to obtain non-radioactive **Cu-MPN** or together with ^{64}CuCl$_2$ (38.11 ± 5.92 MBq, 20 μL in 0.05 M HCl) to obtain ^{64}**Cu-MPN**. The reactions were carried out under vigorous and homogeneous magnetic stirring (750 rpm). After 30 min, the resultant yellowish **In-MPN** or brownish **Cu-MPN** precipitates were collected by centrifugation (5796 g, 1 min) and washed with ethanol and water.

In-MPN: ^{1}H-NMR (250 MHz, MeOD, DCl, δ): 9.16 (d, 2H, C–H$_{imidazole}$ - **L1**), 7.68 (d, 2H, C–H$_{imidazole}$ - **L1**), 7.61 (d, 2H, C–H$_{imidazole}$ - **L1**), 7.56 (s, 4H, C–H$_{aromatic}$ - **L1**), 7.09 (dd, 1H, C–H$_{ring}$ - **L2**), 6.96 (d, 1H, C–H$_{aliphatic}$ - **L2**), 6.83 (dd, 1H, C–H$_{ring}$ - **L2**), 5.56 (s, 4H, C–H$_2$ - **L1**); FT-IR (KBr): 3127 (m, δ(C–H$_{ring}$)), 1625 (s, ν(C=C)), 1584 (m, δ(N–H)), 1519 (s, νC–H$_{ring}$)), 1424 (s, ν(C–O)), 1400 (s), 1237 (s, ν(C–O)), 1106 (m), 1089 (s), 946 (m), 741 (s, δ(N–H$_{ring}$)), 519 (w, In–O) cm^{-1};

Anal. Calcd (%): C 46.25, H 3.93, N 8.03; found: C 45.36, H 3.68, N 8.41. ICP-MS Calcd (%) for **In-MPN**: In 16.45; found: In 17.21. Composition: $In_1L1_1L2_{1.43}(Cl)_2(H_2O)_{0.9}$.

Cu-MPN: ^{1}H-NMR (250 MHz, MeOD, DCl, δ): 9.06 (d, 2H, C–H$_{imidazole}$ - **L1**), 7.61 (d, 2H, C–H$_{imidazole}$ - **L1**), 7.53 (d, 2H, C–H$_{imidazole}$ - **L1**), 7.49 (s, 4H, C–H$_{aromatic}$ - **L1**), 6.98 (dd, 1H, C–H$_{ring}$ - **L2**), 6.86 (d, 1H, C–H$_{aliphatic}$ - **L2**), 6.76 (dd, 1H, C–H$_{ring}$ - **L2**), 5.47 (s, 4H, C–H$_2$ - **L1**); FT-IR (KBr): 3132 (w, δ (C–H$_{ring}$)), 1678 (w), 1625 (m, δ(N–H)), 1521 (s, νC–H$_{ring}$)), 1394 (s, ν(C–O)), 1262 (s, ν(C–O)), 1109 (m), 980 (m), 723 (m, δ(N–H$_{ring}$), 467 (s, Cu–O) cm^{-1}; Anal. Calcd (%): C 50.01, H 4.95, N 6.93; found: C 49.65, H 4.29, N 6.88. ICP-MS Calcd (%) for **Cu-MPN**: Cu 7.87; found: Cu 8.35. Compositional formula: $Cu_1L1_1L2_{1.96}(Cl)_{2.1}(H_2O)_2$.

2.4 Primer coating and PEGylation of MPNs. The synthesized MPNs were redispersed in a vial with 1 mL of phosphate buffer saline (1x PBS, pH 7.4 unless otherwise specified). Subsequently, pyrocatechol (1.7 mg, 10 mmol) and hexamethylenediamine (HMDA, 2.6 mg, 10 mmol) were added under homogenous magnetic stirring (500 rpm) for the formation of the primer coating. The vials were then covered with a pierced Parafilm® (Labbox, Madrid, Spain) in order to allow the entrance of oxygen to the reaction mixture. After 60 min, 2 mg of PEG bis(amine) (3000 MW, Sigma-Aldrich) was added to PEGylate the primer coating; during this step, the vial was sealed and kept under magnetic stirring (500 rpm) for 60 min. Finally, the MPN-PEGs were collected by centrifugation (5796 g, 1 min) and washed three times with water.

2.5 Grafting of MPNs with folic acid. PEG-coated NPs were mixed with 1 mL FA (10 mg/mL in 1x PBS solution) containing n-ethyl-N′-(3-dimethylaminopropyl)carbodiimide (EDC, 12 mg/mL) and *N*-hydroxysuccinimide (NHS, 13 mg/mL). This mixture was ultrasonicated at 60 W for 30 min (Elma Schmidbauer GmbH, Singen, Germany) at room temperature, centrifuged (5796 g, 1 min) and washed with water four times to isolate **In-MPN-FA** NPs.

2.6 Characterization. To assess the feasibility of radiolabeling MPNs and determine the properties of the resultant MPNs, non-radioactive In(III) and Cu(II) salts were used to synthesize MPNs and compared to those radiolabeled with trace amounts of ^{111}InCl$_3$ or ^{64}CuCl$_2$, respectively.

Scanning electron microscopy (SEM) was performed for platinum-metalized samples on a FEI Quanta 650 FEG (Thermo Fisher Scientific, Eindhoven, The Netherlands) in mode operation of secondary electrons with a beam voltage between 5 and 20 kV. Energy-dispersive X-ray (EDX) was measured in non-metalized samples.

FT-IR spectra were recorded on a Tensor 27 FT-IR spectrometer (Bruker Optik GmbH, Ettlingen, Germany) with KBr pellets; all the measurements were taken under atmospheric conditions and data was analyzed with Opus version 7.2 software (Bruker). The size distribution and zeta potential (ζ-potential) of the MPNs were measured using a Zetasizer Nano ZS 3600 and DTS1070 folded capillary cell (Malvern PANalytical, Malvern, UK). The samples for DLS were appropriately diluted and measured in different solvents (1x PBS and water) and over a pH range. Each sample was measured

in triplicate and the resulting DLS data were analyzed using DTS version 7.11 (Malvern PANalytical) software.

Inductively coupled plasma-mass spectrometry (ICP-MS) was obtained using an ICP-MS NexION 300X (Perkin Elmer, San Francisco, CA, USA). All samples were measured in an argon atmosphere. Isotopes of In and Cu were selected as a tracer. The metal concentration of each sample was measured using a calibration curve obtained using 10 aqueous standards in the range of 0.01-250 ppb of metal. All the samples were measured in quadruplicate and analyzed with ICP NexION version 8.2 software (Perkin Elmer).

X-ray photoelectron spectroscopy (XPS) measurements were performed with a Phoibos 150 analyzer (SPECS GmbH, Berlin, Germany) in ultra-high vacuum conditions (based pressure 10^{-10} mbar). Monochromatic Al Kα was used as X-ray source (1486.6 eV). The electron energy analyzer was operated with a pass energy of 50 eV. The analyzer was located perpendicular to the sample surface. The data was collected every eV with a dwell time of 0.5 s and analyzed with CasaXPS version 2.317PR1.1 (Casa Software LTD, Teignmouth, UK).

Powder X-ray diffraction (PXRD) patterns were recorded on PANalytical X'Pert PRO MRD (Multipurpose Diffractometer) (Malvern PANalytical) equipped with a CuKα radiation source ($\lambda = 1.54184$ Å) in four-circle geometry and a goniometer (320 mm radius). The detector used was a Pixel 1D, which is a fast X-ray detector based on Medipix2 technology. The results were analyzed with X'Pert Data Viewer version 1.2d software (Malvern PANalytical).

2.7 Radiochemical characterization and radiochemical purity. The radiochemical yield (RCY) of the radionuclides was determined by recording the activity in the washes compared to that retained on the MPNs using a CRC-55tR dose calibrator (Capintec, Florham Park, NJ, USA). Radiochemical purity was assessed on the final washed particle suspension with an instant thin-layer chromatography (ITLC) system consisting of 150-771 TEC-Control stationary phase (Biodex, Shirley, NY, USA) and an 0.01 M EDTA in 0.9% w/v NaCl mobile phase. The radionuclides stably incorporated within the MPNs stayed at the origin ($R_f = 0$), while the unbound radioactivity moved close to the front ($R_f = 0.9-1.0$). The location and amount of radioactivity on the ITLC was measured using a Cyclone phosphorimager and photostimulable phosphor plate (Packard Instruments, Meriden, CT, USA). ITLC data were integrated using Optiquant software (Packard Instruments).

2.8 Long-term *in vitro* stability. The stability of MPN systems in mouse plasma and whole blood was determined at different time intervals over 7 days. For this purpose, 200 μL of **In-MPN-PEG** and **Cu-MPN-PEG** in 1x PBS at pH 5.2 or 7.4 were incubated with 1 mL of mouse plasma at pH 5.2 or 7.4, respectively (BioIVT, Hicksville, NY, USA) at 37 ºC. The acidification of mouse plasma was achieved by adding a few drops of citrate buffer until reaching the desired pH value. Stability of **In-MPN-FA** and **Cu-MPN-FA** were performed using whole blood extracted from female Balb/c mice and heparin as anticoagulant (BioIVT). For this, 200 μL of **In-MPN-FA** and **Cu-MPN-FA** in 1x PBS were incubated with 1 mL of blood at 37 ºC. All the samples were then placed in

Sectra/Por® dialysis tubing with a molecular weight cut-off (MWCO) of 1-3 kDa (Spectrum, New Brunswick, NJ, USA) and dialyzed against 5 mL of 1x PBS at a pH matching that of the sample. Three aliquots were taken at predefined time points (5 min, 10 min, every remaining 10 min up to 1 h, every 30 min up to 10 h, 12 h, 16 h, 20 h, 1 day, 2 days, 3 days, 5 days and 7 days) and measured by ICP-MS. As controls, uncoated MPNs were analyzed following the same protocol and blanks with PBS-Plasma and blood performed for calibration optimization.

2.9 Cell Culture. Murine colon carcinoma CT26 cell line (ATCC® CRL-2638™), human cervical carcinoma cells HeLa (ATCC® CCL-2™) and the fibroblast cell line NIH/3T3 (ATCC® CRL-1658™) were purchased from Cedarlane (ATCC, Ontario, ON, Canada). The base media for CT26 cells was RPMI 1640 with FA, and Dulbecco's Modified Eagle's Medium (DMEM) for the HeLa and 3T3 cells (Life Technologies, Carlsbad, CA, USA). The base media were all supplemented with 10% fetal bovine serum, 100 U/mL penicillin and 100 μg/mL streptomycin (Life Technologies). All cell cultures were maintained in a humidified incubator at 37°C under an atmosphere of 5% CO_2.

2.10 *In vitro* cell viability studies. CT26, HeLa or 3T3 cells were added to a 96-well plate at a density of 5000 cells per well and allowed to adhere for 24 h. Serial dilutions of MPNs, from 5 - 200 μg of metal/ml, were then added to the wells in quadruplicate and the plate was returned to the incubator. MTT and PrestoBlue™ assays for cell respiration were carried after 24 h of incubation and growth kinetics were monitored using live-cell imaging for upwards of 72 h.

For the MTT assay (CT26), 20 μL of 5 mg/mL thiazoyl blue tetrazolium bromide (MTT, Sigma-Aldrich) solution was added to each well and incubated for 2 h. The supernatant was aspirated without disturbing the cells, and 150 μL of dimethyl sulfoxide (DMSO) was added to each well to dissolve the formazan salts from the metabolism of MTT in metabolically active cells. After complete dissolution, the absorbance was read at 540 nm using a BioTek MX plate reader (BioTek Instruments Inc., Winooski, VT, USA). The percentage of cell viability was calculated by dividing the absorbance of each well by the corresponding value of the control wells only treated with vehicle (1x PBS). A minimum of four independent experiments were performed on different days.

For the PrestoBlue™ assay (HeLa and 3T3), 10 μL of resazurin was added to the media to a final concentration of 15 μM, and the fluorescence was read using a Victor3 plate reader (Waltham, MA, USA) with an excitation wavelength of 531 nm and emission of 572 nm. As with the MTT assay, a minimum of four independent experiments were performed and cell viability was calculated against vehicle-treated cells.

For live-cell imaging, the media in each well was supplemented with 0.25 μmol of YOYO-1 dye (Thermofisher, Burnaby, BC, Canada) and placed into a Incucyte ZOOM (Essen Bioscience, Ann Arbor, MI, USA) housed within a humidified cell incubator. Phase-contrast and green-fluorescent micrographs were taken every 4 h. The data was analyzed using Incucyte ZOOM 2016A software (Essen Bioscience) is reported as phase contrast confluence over time. Representative micrographs

are also provided of the phase-contrast images overlaid with the green fluorescent signal for cell death.

2.11 *In vitro* **cell uptake.** CT26 cells were added to a 24-well plate at a concentration of 50,000 cells per well and incubated for 48 h to allow cells to adhere to the wells. The media was then carefully removed and the cell monolayer was washed with 500 μL 1x PBS followed by complete media; the base media was switch, however, to RPMI 1640 media without FA (Life Technologies) to avoid saturation of the FA-receptors on the cell with the targeting ligand on the MPNs. Radiolabeled particles diluted in complete media were added to the cells to achieve a final concentration of 4.16 μg of **^{111}In-MPN-FA** or 8.3 μg of **^{64}Cu-MPN-FA** per well. The amount of radioactivity per well was 59.2 kBq of **^{111}In-MPN-PEG**, 88.1 kBq of ^{111}**In-MPN-FA**, 46.6 kBq of ^{64}**Cu-MPN-PEG** and 55.9 kBq of ^{64}**Cu-MPN-FA**. At 0, 0.08, 0.25, 0.5, 1, 2, 5 and 24 h, the media was collected, and the cells were washed with ice-cold 1x PBS. Afterward, the cells were treated with a sodium dodecyl sulfate (SDS)-NaOH lysis buffer (0.25% w/v SDS in 0.05 M NaOH) to release the internalized NPs, and the solution was collected. The activity present in the media and 1x PBS (extracellular fraction) and the lysis buffer (intracellular fraction) were then quantified with a 2470 Wizard2™ gamma counter (PerkinElmer) recording counts per minute of photons (cpm) in the following energy windows: 140 - 200 keV (for ^{111}In), and 400–600 keV (for ^{64}Cu). Each time point was performed in triplicate.

2.12 Animal Care and Ethics Statement. The current study was performed in accordance with the Canadian Council on Animal Care (CCAC) and a protocol (A16-0150) approved by the Animal Care Committee (ACC) of the University of British Columbia. Seven-week-old female Balb/c mice were purchased from Charles River Laboratories (Sherbrooke, QC, Canada). Mice were allowed to acclimatize to the facility for a minimum of 1 week before experimental use. The animals had unlimited access to food, water and enrichment during the course of the study and were never housed singly for companionship.

2.13 Animal Models. For tumor inoculation, CT26 cells were harvested with trypsin-EDTA (Life Technologies) and washed thrice with 1x PBS before being suspended at a concentration of 2.24×10^7 cells/mL in 1x PBS. Each mouse was injected subcutaneously onto the right shoulder with 0.1 mL of the cell suspension. The animals had been shaved at that site the day before and the injection site was wiped with 70% v/v ethanol before injection. For three weeks, total mouse body weight and tumor size (width (W) and length (L) by caliper measurement) was recorded every other day. Tumor volumes were calculated using the formula $(L \times W^2)/2$. Imaging was initiated when tumor volume reached 300-500 mm^3 (approx. 3 weeks after the implantation) and n = 3 mice per group were used.

2.14 SPECT/PET/CT Imaging. Mice bearing CT26 tumors were anesthetized using isoflurane on a precision vaporizer (5% in oxygen for induction, between 1.5 and 2.5% in oxygen for maintenance) and received a subcutaneous injection of 0.5 mL lactated Ringer's solution (Baxter, Deerfield, IL, USA) for hydration prior to radiotracer administration and each subsequent scan. After the induction of anesthesia, an injection containing 100 μL of **^{111}In-MPN-PEG** (0.18 ± 0.03 μg

metal/mL; 0.57 ± 0.04 mg/mL; Group 1), **¹¹¹In-MPN-FA** (0.17 ± 0.05 µg metal/mL; 0.72 ± 0.06 mg/mL; Group 2) or **⁶⁴Cu-MPN-PEG** (0.25 ± 0.07 µg metal/mL; 0.24 ± 0.02 mg/mL; Group 3) in 1x PBS was administered via tail vein to each animal. Average injected activities were 1.04 ± 0.11 MBq, 1.44 ± 0.08 MBq and 1.02 ± 0.69 MBq for Group 1, 2 and 3, respectively. Immediately after injection, dynamic SPECT/CT images were acquired for the first hour in 15 min frames followed by static scans at 5 and 24 h using a VECTor/CT scanner (MILabs, Utrecht, The Netherlands)[55] equipped with a high-energy ultra-high-resolution mouse pinhole collimator (HE-UHR-1.0 mm). Following each SPECT or PET acquisition, a whole-body CT scan was acquired to obtain anatomical information. CT scans were acquired with a tube setting of 55 kV and 615 µA. Throughout the entire scanning procedure, mice were kept under anesthesia with 1.5% isoflurane in oxygen, and the body temperature was maintained constant using an integrated heating pad in the scan bed. After each scan, the animals were recovered individually with heat support and nearby access to a HydroGel® gel-based water source (ClearH₂O, Portland, ME, USA). Once recuperated from anesthesia, the animals were returned to their normal group housing until their next scan.

Images were reconstructed using pixel-based ordered-subset expectation maximization (POSEM)[56] algorithm that included resolution recovery and compensation for distance-dependent pinhole sensitivity, using 16 subsets, 6 iterations (96 ML-EM equivalent) and an isotropic 0.4-mm voxel grid. A 20% ¹¹¹In photopeak was centered at 171 keV. Similarly, a 20% ⁶⁴Cu photopeak was centered at 511 keV. All images were decay-corrected and, using the CT image, attenuation correction was applied. CT projection data were reconstructed using SkyScan NRecon software (Micro Photonics Inc, Allentown, PA, USA) to generate a 3D CT image on 0.169 mm³ voxel grid.

To calculate the uptake of radiolabeled MPNs in the organs of interest, the registered images were analyzed using AMIDE v. 1.0.5 (Los Angeles, CA, USA). Various volumes of interest (VOIs) of ~2-3 mm³ were drawn manually inside each organ to determine the time-activity pattern per target organ. Thus, the delineated regions were lungs, liver, spleen, bladder, tumor and bone. The uptake was expressed as Standardized Uptake Value (SUVs). To relate the scanner units (counts/voxel) to radioactivity concentration (MBq/mL), a calibration factor was determined by scanning a point-source phantom with a known concentration of ¹¹¹In or ⁶⁴Cu. Representative maximum-intensity projection (MIP) renderings over time were prepared using AMIDE software; a 3D Gaussian filter was applied to the SPECT data set for added clarity.

2.15 *Ex vivo* Biodistribution. Following the final imaging scan, each mouse was sacrificed by CO₂ asphyxiation under isoflurane anesthesia. The cardiac puncture was promptly performed to recover blood, and the organs of interest were harvested, rinsed with 1x PBS and blotted dry. Each organ was weighed, and the radioactivity of the collected tissue was measured using a calibrated Packard Cobra II 5010 gamma counter (Perkin Elmer), recording counts per minute of photons (cpm) in the following energy windows: 140 - 200 keV (for ¹¹¹In), and 400–600 keV (for ⁶⁴Cu). Counting was performed immediately following sacrifice. Counts were decay corrected to the time of injection.

A calibration factor was applied to convert cpm values into units of radioactivity (MBq). Data were corrected for organs that could not be entirely removed (blood, muscle, bone) using standardized organ weights for the age- and sex-matched mice.[57] Data are reported as the percentage of the injected dose per gram (% ID/g) and per organ (% ID/organ).

2.16 Statistical Analysis. All data are expressed as mean ± SD unless stated otherwise of at least three experiments. GraphPad Prism software (Graphpad Software Inc, La Jolla, CA, USA) was used to perform all statistical analyses. Comparison was made by two-way ANOVA and multiple comparisons were performed by Sidak's post-test. A value of $p < 0.05$ was considered significant.

3. RESULTS AND DISCUSSION

3.1 Synthesis and Characterization of In-MPN and In-MPN-PEG. The one-pot reaction of $InCl_3$ with the **L1** imidazole and the **L2** catechol as co-ligands in a 1:1:2 molar ratio (**Figure 1**) yielded a yellowish precipitate after vigorous stirring at room temperature. SEM images revealed spherical **In-MPN** NPs, with average sizes of 74 ± 17 nm (**Figure 2**). The result from the DLS measurement in 1x PBS were similar, with a hydrodynamic diameter of 87 ± 11 nm (**Figure 2**). The absence of diffraction peaks observed by PXRD indicated the amorphous nature of the NPs (**Figure S1**). The chemical structure of **In-MPN** was characterized by different complementary techniques such as FT-IR, EDX, XPS, ^{1}H-NMR and ICP-MS. FT-IR spectroscopy corroborated the coordination between the metal and the ligands (**Figure S2a**); the frequency intensity decrease of the bands at $\nu = 3000\text{-}3500$ cm^{-1} was attributed to deprotonation of catechol groups (–OH) present in **L2**. Besides, a new vibrational band assigned to the C–O stretching of the catecholate moiety bonded to metal centers appeared in the range of 1400-1420 cm^{-1}. The broadband around 730-740 cm^{-1} could be attributed to the deformation of the imide-five-ring from the **L1** ligand due to its coordination to the corresponding metals. Additionally, typical vibrational bands of **L1** ($\nu = 1520, 1232, 1105$ cm^{-1}) were also observed in the IR spectra. The presence of In and the Cl$^-$ counter-anion were corroborated by EDX and XPS, which also confirmed the expected oxidation states of In(III) (**Figure S3**, **S4a** and **S4b**). ^{1}H-NMR (**Figure S5**) of the dissolved NPs was used to calculate the ratio of the ligands and ICP-MS to measure the metal percentage (**Table S1** and **S2**). Both results, together with the elemental analysis of C, N and H content (**Figure S6**), resulted in a tentative compositional formula for **In-MPNs** of $In_1\textbf{L1}_1\textbf{L2}_{1.4}Cl_2(H_2O)_{0.9}$. This final formula differed from the expected values for an initial stoichiometry of $In(III)_1\textbf{L1}_1\textbf{L2}_2$, as previously described for related nanoscale coordination polymers.[7,58] The reason for this is the out-of-equilibrium conditions used for the reaction that favor: i) the formation of different oligomeric species, ii) the encapsulation of free ligand and/or solvent molecules within the particles and iii) a combination of both. It is worth mentioning that the results were fully reproducible over three different batches of the same NPs, confirming the robustness of the process yielding defined NPs.

After full characterization, the colloidal stability of the MPNs was determined in solution at different pH values. The size and ζ-potential of **In-MPNs** were first measured in water over a pH range of 5-9 (**Figure S7**). It might be worth noting that the MPNs undergo a fast and irreversible decomposition at pH's lower than 4 and higher than 10. When the pH was acidified to pH 5, **In-MPNs** tended to aggregate (221 ± 9 nm) due to the reduction of the ζ-potential to -2.3 ± 1.2 mV as a consequence of the gradual protonation of the carboxylic acid groups of **L2** located on the surface of the **MPNs**. When the pH becomes basic, the DLS measurements indicated a decrease in size until it becomes almost constant at pH 8-9 (81 ± 7 nm); the ζ-potential at this pH range was solidly negative (-34.2 ± 3.1 mV) due to the deprotonation of the same carboxylic groups described above. At pH 7.4, the ζ-potential was still negative (-23.9 ± 2.2 mV) and the NPs had an average diameter of 87 ± 11 nm. **In-MPN** thus exhibited good colloidal dispersion at physiological pH, although they started to aggregate and precipitate after 6 h (**Figure S8a**).

To confer more biostability and biocompatibility, **In-MPN** NPs were functionalized with a PDA-like coating using a methodology previously reported[48] and subsequently PEGylated through a condensation reaction with amine groups (**Figure 1**). The resulting **In-MPN-PEG** showed a size increase up to 120 nm, as observed in the solid-state by SEM (**Figure 2**). DLS measurements in 1x PBS showed a similar size of 123 ± 6 nm with a narrow size distribution (PDI < 0.20). PEGylation also induced a notable modification of the surface charge as measured by ζ-potential, moving from the negative values obtained for the uncoated NPs to positive values (~30 mV) after the coating (**Figure S7**). Coupling hydrophilic PEG chains to the surface carboxylic groups also reduced the overall pH effect (**Figure S7**) while favoring longer colloidal stabilities than those reported for **In-MPN** under the same physiological conditions (**Figure S8**). Additional chemical analysis confirmed the attachment of the PEG units; for example, the elemental analysis showed an increase in the percentages of C and H as expected (**Figure S6**). In the same way, the coating and PEGylation of the **MPNs** were confirmed by FT-IR. The spectra clearly showed the appearance of intense bands at ~2900 cm^{-1} and ~1150 cm^{-1} corresponding to the C–H bonds from the alkyl chain and the stretching vibration of C–O–C, respectively (**Figure S2b**).

3.2 Functionalization of MPNs with Folic Acid (In-MPN-FA). To improve the targeting properties, FA molecules were covalently coupled to the accessible amine-terminated PEG chains (**Figure 1**). For this, a carbodiimide assisted coupling reaction was performed between the terminal amine groups of PEG and carboxylic groups of FA. The post-functionalization of the PEGylated MPNs was preferred instead of the pre-functionalization of PEG chains before MPNs synthesis to ensure the presence of FA on the surface of NPs and to maximize their interaction with FA-receptors. After functionalization with FA, no appreciable changes in size and colloidal stability were observed in the **In-MPN-FA** compared to the **In-MPN-PEG** (**Figure 2** and **Figure S9).**
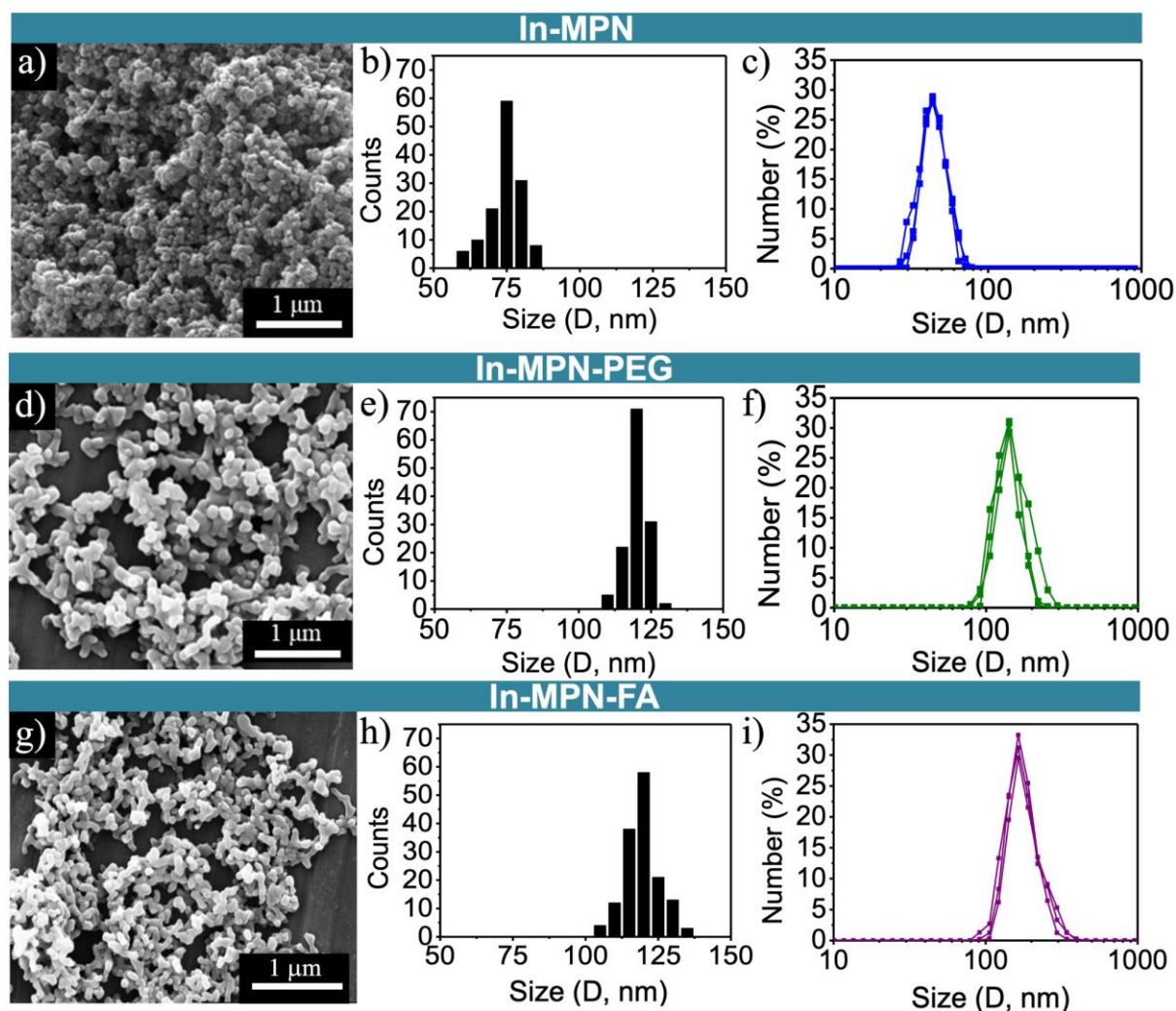
Figure 2. Morphological and size characterization for **In-MPN** (top), **In-MPN-PEG** (middle) and **In-MPN-FA** (bottom). (a, d, g) Scanning electron microscopy (SEM). (b, e, h) Size distribution histogram from SEM measurements. (c, f, i) Size distribution of colloidal dispersions in PBS measured by dynamic light scattering (DLS)

3.3 Biodegradability of In-MPN, In-MPN-PEG and In-MPN-FA. Biodegradability of the MPNs, with and without the PEG coating, was studied under physiological conditions (incubation in diluted mouse plasma at pH values of 7.4 and 5.2 (**Figure S10a,b**) at 37°C for 7 days). Experiments were carried out using a dialysis bag, with the metal concentration in the dialysate quantified over time using ICP-MS. Both uncoated and PEGylated **In-MPNs** slowly released indium metal ions into the surrounding media. It took about 7.5 h to release 50% of the metal for the uncoated NPs at physiological pH, being notably faster when the pH was decreased (4.5 h for pH 5.2) (**Table S3**). For coated MPNs, the time needed for the 50% of metal release was 21 h for **In-MPN-PEG** at pH 7.4 (**Table S3**). In a more acidic environment, pH 5.2, it took 12 h for 50% of the metal to be released from the **In-MPN-PEG** particles. In order to confirm the stability of **In-MPN-FA**, biodegradability experiments were performed using blood extracted from a Balb/c mouse (**Figure S10c**) in order to simulate a more realistic *in vivo* environment. Interestingly, the obtained results

showed similar metal-release profiles where the 50% of In(III) was measured after 20 h (**Table S3**). These results confirmed the influence of the coating, allowing for more gradual and controllable biodegradation of the synthesized MPNs in a biological milieu over a range of pH values. The particles were also determined to be stable enough for use *in vivo*, such as an imaging study, but degraded fast enough to prevent unwanted particle accumulation with time (*vide infra*).

3.4 Cell toxicity of In-MPN, In-MPN-PEG and In-MPN-FA. The potential toxicity of **In-MPN** and **In-MPN-PEG** was tested in HeLa, CT26 and 3T3 cells at different concentrations (**Figure 3**). Over 24 h, no change in cellular respiration, a measure of cell toxicity, was observed in CT26 or HeLa cells at any concentration of uncoated and coated **In-MPN**s. However, a significant decrease in respiration (~60-70% of media control) was observed in the 3T3 cell line for uncoated **In-MPN**s above 75 μM. The PEG coating, with or without FA functionalization, prevented this toxicity at metal concentrations up to 200 μM, illustrating the importance of the coating for biocompatibility. Live cell phase contrast imaging of CT26 cells incubated with **In-MPN-PEG** or **In-MPN-FA** at 10 μM metal concentration confirmed normal cell growth kinetics during the incubation period without any overt signs of agglomeration or aggregation of the NPs in the media (**Figure S11**). There was also no increased signal from the YOYO-1 live/dead markers in the MPN-treated cells when compared to vehicle-treated controls (**Figure S11**). Thus, the phenol-based polymeric coating increased their biocompatibility for all three cell lines tested.
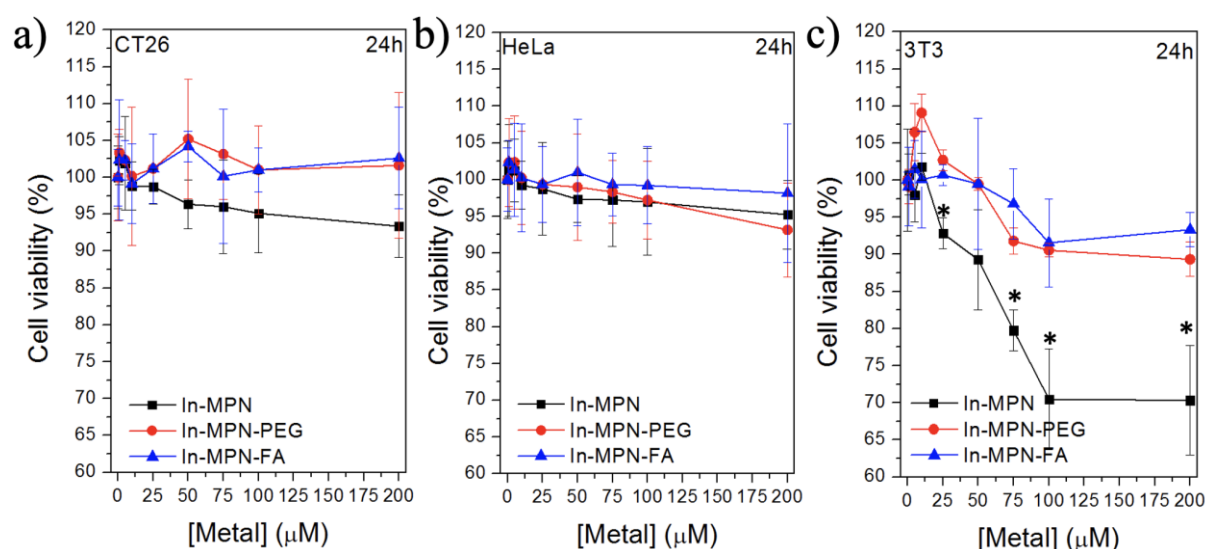

Figure 3. Concentration-dependent cytotoxicity effects of MPNs were evaluated for 24 h with uncoated **In-MPN**, PEG-coated **In-MPN-PEG** and **In-MPN-FA** in 3 different cell lines: (a) CT26, (b) HeLa and (c) 3T3. Cell viability was assessed using an MTT assay for the CT26 line and a PrestoBlue[TM] assay for the HeLa and 3T3 lines. *p < 0.05 when comparing **In-MPN** with **In-MPN-PEG** and **In-MPN-FA**.

3.5 Intracellular Uptake of In-MPN-PEG and In-MPN-FA. The synthesized **In-MPNs** were successfully radiolabeled with ^{111}In via a chelator free method with a radiochemical yield (RCY) of

14

71 ± 4% and 69 ± 2% for **In-MPN-PEG** and **In-MPN-FA**, respectively (**Tables S4** and **S5**). RCY refers to the fraction of the radioactivity that has been stably incorporated into the NPs in comparison to the starting amount. The RCY was significantly higher than previously reported for other nanosystems,[59] which could allow for a reduction in the dose of NPs required for an imaging procedure and mitigate the risk of adverse effects. A high degree of radiochemical purity, over 97%, was achieved for all ^{111}In-MPN derivatives prepared. This adds confidence that the radioactive signal observed *in vivo* was from the NPs and not due to free radiometal.

Before going *in vivo*, the effect and the role of the FA on cellular uptake was assessed in CT26 cells, a colorectal cancer cell line well-known to overexpress FA-receptors.[60] Both **In-MPN-PEG** and **In-MPN-FA** were incubated for 24 h with the cells and the cellular uptake was evaluated by gamma counting (**Figure 4**). The experimental results showed a higher degree of uptake for the **In-MPN-FA** compared to **In-MPN-PEG**. FA-conjugation increased internalization from 2 h of incubation onward, with In-MPN-FA reaching 14% higher uptake than **In-MPN-PEG** at 24 h (**Table S6**). The results show how cellular uptake could be improved by engineering the MPNs surface with the targeting moiety. Considering that a significant difference between the two MPNs was not observed before 2 h incubation, this active targeting might only be relevant *in vivo* for NPs that circulate in the blood pool for a considerable amount of time. This result correlated with the *in vivo* findings in downstream experiments, which showed an increased tumor uptake of **In-MPN-FA** compared **to In-MPN-PEG** at later timepoints.
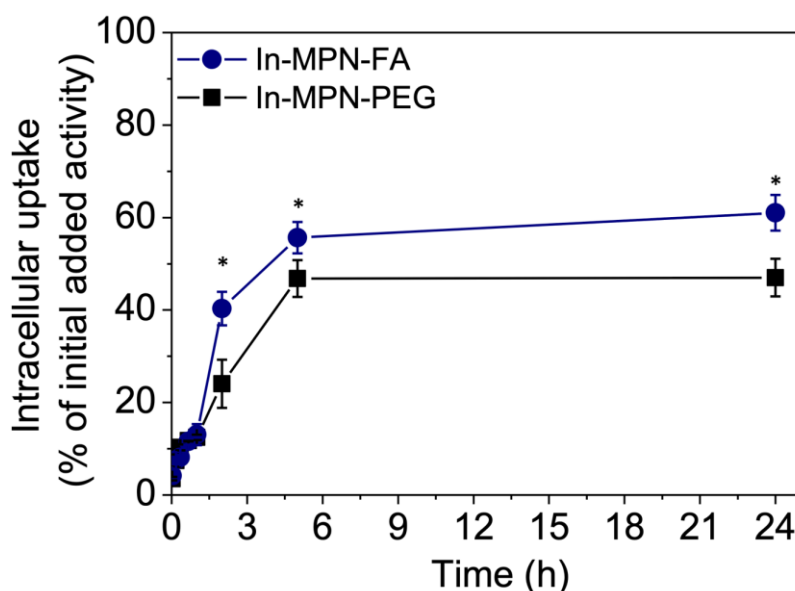
Figure 4. Intracellular uptake of **In-MPN-PEG** (black squares) and **In-MPN-FA** (blue circles) into CT26 cells, characterized for its overexpression of FA receptors. *p < 0.05 in comparison between **In-MPN-PEG** and **In-MPN-FA**.

3.6 *In vivo* Imaging and Biodistribution Analysis of In-MPN-PEG and In-MPN-FA. Quantitative *in vivo* SPECT/CT images were acquired over a period of 24 h in order to assess the biodistribution and pharmacokinetics of both non-targeted (**In-MPN-PEG**) and targeted (**In-MPN-FA**) NPs after i.v. administration. **Figure 5** shows representative maximum intensity projections (MIP) of **In-MPN-PEG** (**Figure 5a**) and targeted **In-MPN-FA** (**Figure 5b**) from each scan time point in CT26-tumor-bearing Balb/c mice. Simultaneously, quantified uptake values of both radiolabeled MPNs in multiple organs of interest represented as mean standardized uptake values (SUV$_{mean}$) are depicted in **Figure 5c**. It should be noted that a small amount of radioactivity (~0.4%) was excreted over the first ~ 1 h of the scan series in both groups. This signal likely represented a small amount of non-complexed ^{111}In(III) in the final particle suspension, seeing how radiopurity was only 97%. We have previously observed this excretion pattern for ^{111}InCl$_3$ when administered i.v. beforehand.[61]

Beyond this aspect, and upon receiving similar doses of labeled MPNs, an initial inspection of *in vivo* SPECT/CT images showed a very similar pattern of distribution for both groups of MNPs, that is, a rapid accumulation and predominance in the lungs immediately following i.v. administration. Quantitatively, about 80% of the total **In-MPN-FA** dose was retained in the lungs 5 mins after injection, which decreased to about 12% at 24 h. On the other hand, approximately 30% of the injected dose **In-MPN-PEG** could be found in the lungs at the earliest time point, which decreased to 3% by the final scan. The lung distribution pattern may be explained by the agglomeration of the MPNs when injected into the blood and subsequent entrapment in the lung endothelium.[62] The first capillary bed reached following an i.v. injection is in the lung, and any particulates larger than the diameter of those vessels (~5-8 μm)[63,64,65] will become mechanically trapped there. This is the principle behind lung perfusion imaging, for example, with agents such as ^{99m}Tc-labeled macroaggregated albumin.[66] The higher degree of uptake and a longer period of retention in the lungs for **In-MPN-FA** may also relate to the presence of FA-receptors in the lung endothelium.

Soon afterward, the nanomaterial was mechanically filtered, allowing MPNs, and some possible resultant metabolites, further circulation in the bloodstream and final clearance through the reticuloendothelial system (RES), leading to an increased concentration in the liver and spleen according to their hydrodynamic diameter. This is not surprising as these organs making up this system are rich in phagocytic cells and are well-known to effectively remove particulates from the bloodstream.[67,68] Kidney and bone uptake increased over the course of the imaging study, which was consistent with the distribution pattern of released ^{111}In(III) from the MPN matrix.[61]
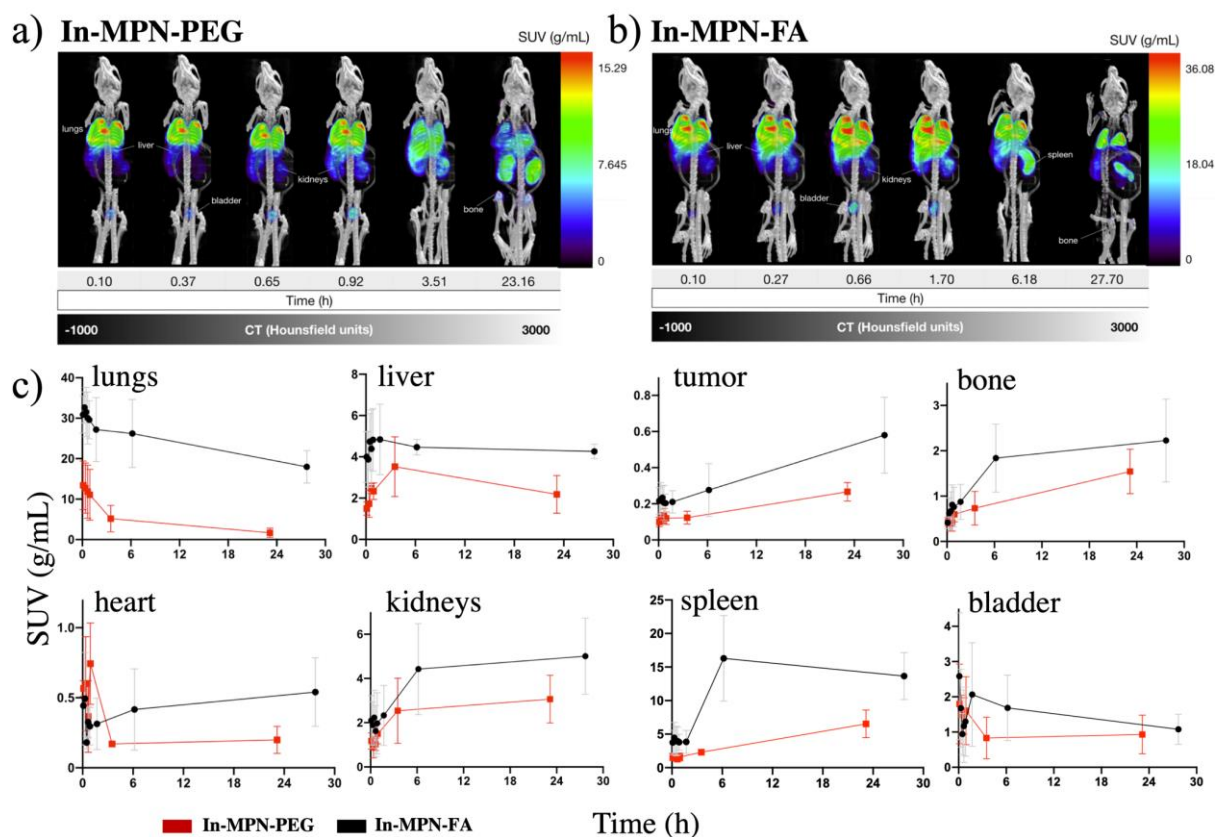
Figure 5. Top view maximum intensity projections (MIPs) of total body SPECT/CT scans over 24 h after intravenous (i.v.) administration of (a) **In-MPN-PEG** and (b) **In-MPN-FA**. (c) Standardized uptake values (SUVs) for the main organs are given for **In-MPN-PEG** (in red) and **In-MPN-FA** (in black). Data is presented as mean ± SD (n=3).

Although both ^{111}In-labeled MPN derivates were rapidly cleared from the blood, limiting their ability to target the tumor, there is evidence that the addition of the FA-moiety to the surface of the particles had an active targeting effect. Uptake and delineation of the CT26 tumor, which overexpresses FA-receptors, was clearly observed in the renderings of the **In-MPN-FA** group at 24 h post-injection (**Figure 6**). Much lower tumor uptake was observed for the **In-MPN-PEG** group in all the images recorded during this study, indicating a minor ability for these nanoparticles to accumulate in the tumor. The differential retention and accumulation of both families of NPs were further confirmed with the post-mortem biodistribution data. Higher accumulation of **In-MPN-FA** (1.33 ± 0.09 %ID/organ, 12.55 ± 9.92 %ID/g) was observed in comparison to **In-MPN-PEG** (0.19 ± 0.05 %ID/organ, 1.25 ± 0.47 %ID/g) in tumor tissues. Together, these results confirmed the importance of actively targeting MPNs to enhance accumulation at the desired site, a tumor, in this case, over-relying simply on the passive accumulation with PEG-functionalized counterparts. These results suggested that FA is a suitable targeting agent for active target-directed accumulation.
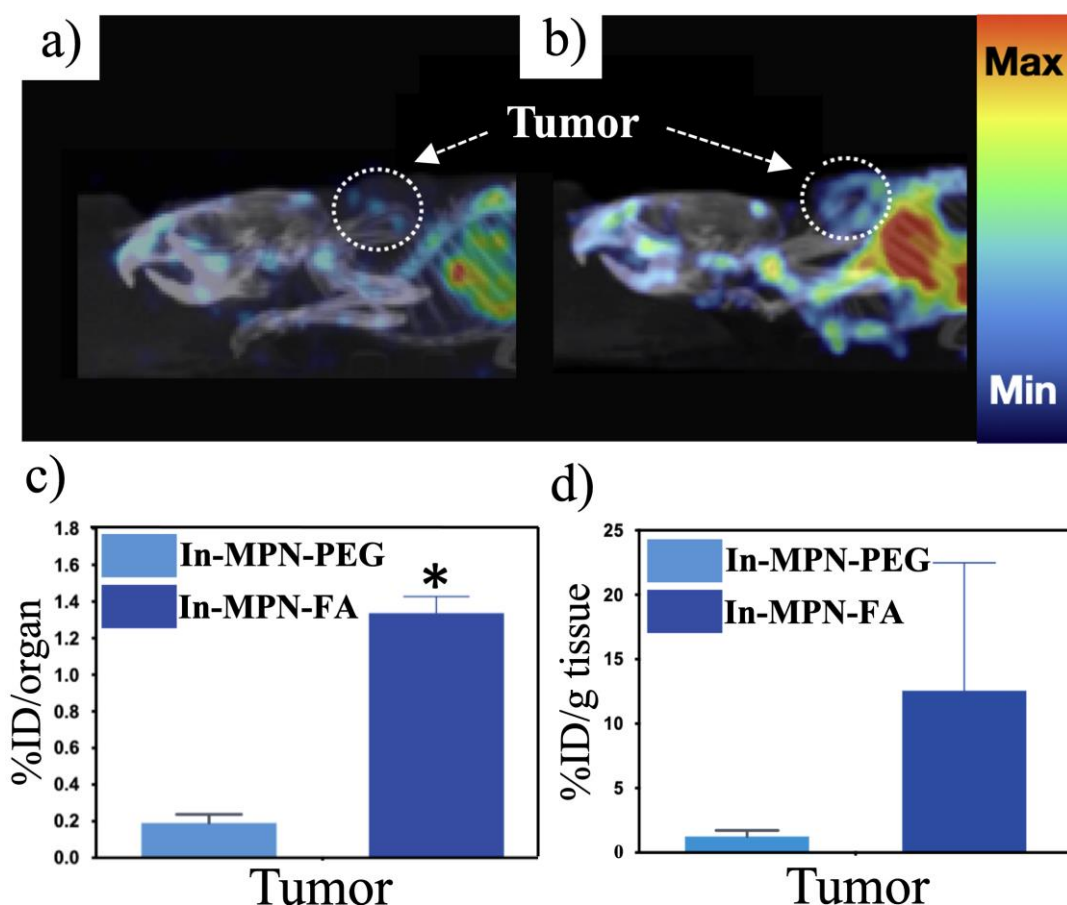
Figure 6. SPECT/CT fused MIP images of a Balb/c mouse bearing a CT26.WT xenograft 24 h after i.v. injection of (a) **In-MPN-PEG** and (b) **In-MPN-FA**. The tumor is indicated with an arrow and dashed circles. Quantitative biodistribution of **In-MPN-PEG** (in blue) and **In-MPN-FA** (in navy blue) at 24 h post-injection expressed as (c) % of ID per organ, and (d) % of ID per gram of tissue. The values are represented as mean ± SD with n = 3 mice per group. *$p < 0.05$ in comparison of **In-MPN-FA** with **In-MPN-PEG**.

To further investigate the biodistribution of these NPs, *ex vivo* biodistribution studies were also performed for the other organ system besides the tumor at 24 h post-injection. As shown in **Figure 7** and **Table S7**, both NP groups were excreted through the liver and renal system. Besides, they shared comparable biodistribution patterns, where the major retention of the NPs remained in the lungs, kidneys, spleen, liver and bone at 24 h post-injection (**Figure 7** and **Table S7**). The accumulation of **In-MPN-PEG** in the lungs (18.55 ± 2.27 %ID/g), kidneys (20.05 ± 1.64 %ID/g), liver (13.41 ± 2.60 %ID/g) and spleen (37.20 ± 3.62 %ID/g) was significant after 24 h p.i. Albeit the retention was comparable for the two groups, the average %ID/g in the tumor excised from those mice injected with **In-MPN-FA** was higher (12.55 ± 9.92 %ID/g) compared to that of **In-MPN-PEG** (1.25 ± 0.47 %ID/g).

In corroboration with the SPECT data set, the amount of activity in the lungs of the **In-MPN-FA** animals (4.26 ± 0.35 % ID/organ) was statistically higher than that of the untargeted counterpart (2.70 ± 0.27 % ID/organ). Appreciable tissue concentrations and total organ uptake were further observed for both NP groups in the blood, kidney and bone. Kidney uptake, both as % ID/g and % ID/organ,

for the ^{111}In-MPN-PEG particles was statistically higher than the **In-MPN-FA** group though. Uptake into other organ systems measured, such as the heart tissue and intestines, was minimal. Worth to mention, the grafting with FA increased the retention time of the NPs in the lungs and changed the clearance behavior as observed in significant differences when compared both **In-MPN-PEG** and **In-MPN-FA** systems (**Figure 7**).
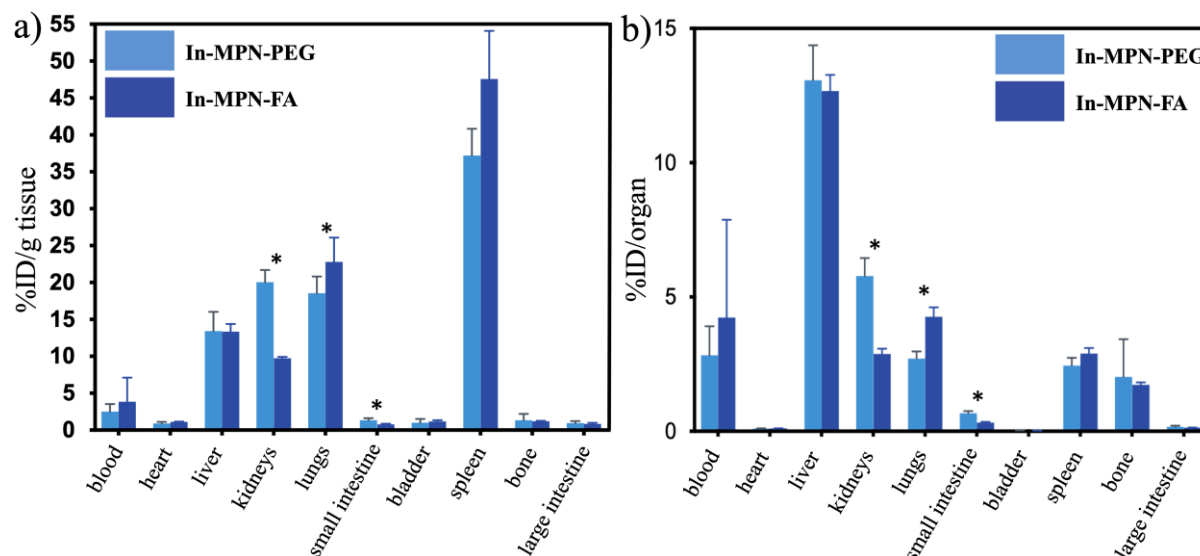
Figure 7. Quantitative biodistribution of **In-MPN-PEG** (in blue) and **In-MPN-FA** (in navy blue) at 24 h post-injection expressed as (a) % of ID per g of tissue, and (b) % of ID per organ. Data is presented as mean $\pm$ SD (n=3). *$p < 0.05$ in comparison between **In-MPN-PEG** and **In-MPN-FA**.

3.7 Synthesis, Characterization and PET Study of Cu-MPN-PEG. In order to validate our platform for PET imaging, we synthesized analogous **Cu-MPN-PEG** NPs. The incorporation of ^{64}Cu in the MPNs would enable their evaluation as PET probes, and would offer a broader scope of these nanoconstructs as multimodal imaging agents. The synthesis of **Cu-MPN-PEG** NPs was performed following the same methodology described for **In-MPN-PEG** (**Figure 1**). Overall, the reaction of $CuCl_2$ with **L1** and **L2** ligands in a 1:1:2 molar ratio yielded PDA-like polymer-coated **Cu-MPN** (**Cu-MPN-PEG**) NPs (**Figure 8d**) sized 119 ± 10 nm by SEM. DLS measurements in 1x PBS were in agreement, showing a hydrodynamic diameter of 127 ± 8 nm and narrow size distribution (PDI < 0.20) (**Figure 8f**). The chemical structure and formation of MPNs were characterized by different complementary techniques such as XRD, FT-IR, EDX, XPS, ^{1}H-NMR and ICP-MS (**Figures S12, S13, S14, S15, S16, S17** and **Tables S8** and **S9**). The results confirmed the versatility of these MPNs to incorporate different metals yielding similar chemical structures and properties compared to its **In-MPN** analog. Even the compositional was very close to that obtained for the In(III) analog: $Cu_1\mathbf{L1}_1\mathbf{L2}_{1.96}Cl_{2.1}(H_2O)_2$ formula.
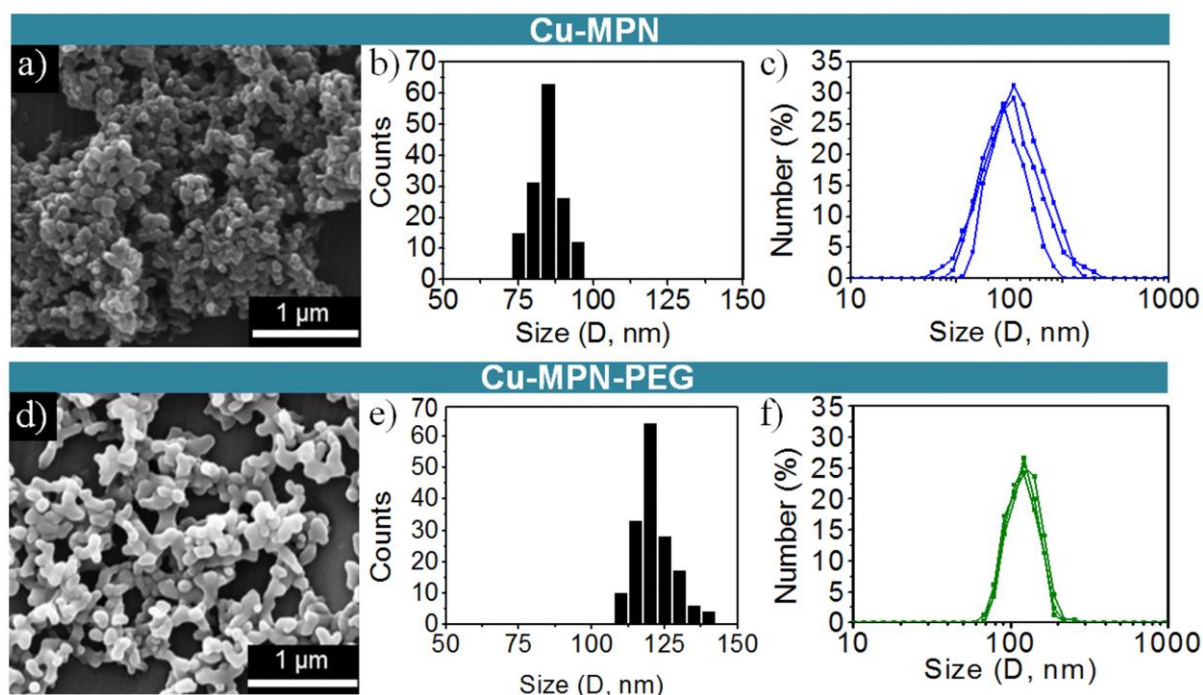
Figure 8. Morphological and size characterization for **Cu-MPN** (top) and **Cu-MPN-PEG** (bottom). (a, d) SEM images. (b, e) Size distribution histogram from SEM measurements. (c, f) Size distribution of colloidal dispersions in PBS measured by DLS.

Interestingly, the coating of **Cu-MPN** with the PDA-like polymer and additional PEGylation induced similar changes in terms of biostability and biocompatibility compared to its analog **In-MPN**. In this case, the coating caused a surface charge measured by ζ-potential of ~ 30 mV, leading to the formation of long-term stable colloidal dispersions in physiological solutions compared with uncoated MPNs (**Figure S19**). Moreover, the coupling of hydrophilic PEG chains to the surface carboxylic groups reduced the number of protonable moieties and increased the positive charge while decreasing the effect of pH in the colloidal dispersion (**Figure S18** and **S19)**. The chemical stability and biodegradation of **Cu-MPN-PEG** were studied by dialysis in physiological conditions (incubation in diluted mouse plasma at pH values of 7.4 and 5.2 (**Figure S20a,b**) at 37°C for 7 days). At physiological pH, the time needed for the 50% of metal release was 19 h, which was reduced to 10 h at pH = 5.2 (**Table S10**), indicating a very comparable metal release profile as with its In(III) analogs. As a further step, the biodegradability of functionalized **Cu-MPN-FA** was evaluated (**Figure S20c**). When analyzing the stability in blood, similar results were found, where 50% of Cu(II) ions were released after 17 h (**Table S10**). Cell toxicity was also evaluated in HeLa, CT26 and 3T3 cell lines over 24 h (**Figure S21**). Coated **Cu-MPN-PEG** showed lower toxicity (86% and 91% cell viability at 50 μM metal in HeLa and 3T3 cells, respectively) compared to the same NPs when tested in CT26 cells (76% cell viability at 50 μM metal). With increasing metal concentration, cytotoxicity increased as well for the Cu-MPNs. Toxicity was consistently higher than that observed with the In-MPN counterparts, presumably due to the increased toxicity of Cu(II) ions over In(III) ions. However, cell viability never decreasing below 68% for any of the Cu-MPNs tested in any cell line, even at the

highest concentration (200 μM metal). Differences in the toxicity between **Cu-MPN** and **Cu-MPN-PEG** were observed in all cell lines but in particular 3T3. The reduced toxicity observed with **Cu-MPN-PEG** was likely due to the increased stabilization of the NP, thus slowing the biodegradation process and release of toxic Cu(II) ions.

Interestingly, when the effect of the FA on cellular uptake was evaluated, **Cu-MPN-PEG** and **Cu-MPN-FA** again showed similar behavior compared with its **In-MPN** analogous (**Figure S23** and **Table S13**). These results confirmed the versatility of these MPNs to incorporate different metals while retaining similar features.

The RCY for **Cu-MPN-PEG** was 87 ± 2% after all the washing steps (**Table S11** and **S12**). The radiochemical purity was sufficiently high to proceed *in vivo*, exceeding 95%. However, a major concern with injecting **Cu-MPN-PEG** was toxicity, arising from the increased toxicity signal observed with the particles *in vitro*. Subsequently, a lower dose of particles was administered compared to the **In-MPN-PEG** group (injected dose of 0.52 mg MPNs/mL and 0.45 mg MPNs/mL for **In-MPN-PEG** and **Cu-MPN-PEG**, respectively)**.** As with **In-MPN-PEG**, **Cu-MPN-PEG** analogous showed a strong PET signal in the lungs. **Figure S24** shows a representative MIP rendering following i.v. administration of **Cu-MPN-PEG** into a Balb/c mouse 15 min post-injection. Unfortunately, acute respiratory distress was observed in the animal after that scan, which reached the humane endpoint and the end of the experiment. Although the obtained image validated the potential use of these nanosystems to integrate different radiometals for both PET and SPECT imaging, further refinement of **Cu-MPN-PEG** will be required to ensure the feasibility and the safety of these NPs as diagnostic or therapeutic entities.

To circumvent this limitation, the injected doses were reduced to a lower number of NPs, too low for imaging, but adequate for *ex vivo* biodistribution studies at 5 h post-injection (injected dose of 0.12 mg MPNs/mL) to continue the pharmacokinetic assessment with these NPs. Although the radioactive dose was now too low to carry out PET imaging, an *ex vivo* biodistribution study was performed instead. Though the biodistributions were initially planned to be carried out at 24 h post-injection like the ^{111}In-MPN counterparts, and the mice showed no overt clinical signs of toxicity, the animals were prematurely sacrificed at 5 h post-injection as a precaution. Post-mortem quantitative analysis of the organs expressed in %ID/organ and %ID/g of tissue are presented in **Figure 9** and **Table S14**. After 5 h post-injection, the NPs were still mainly in the lungs (55.02 ± 3.43% ID/g) and blood (18.44 ± 3.48% ID/g). At that time point, lower levels of uptake were observed in the liver (4.37 ± 0.20% ID/g), small intestine (0.61 ± 0.015% ID/g), kidneys (0.93 ± 0.09% ID/g) and spleen (0.59± 0.09% ID/g) (**Figure 9** and **Table S14**). Interestingly, we observed low tumor uptake (3.72 ± 1.36% ID/g, 0.39 ± 0.01 % ID/organ) at 5 h post-injection.

With this preliminary data, we could study for the first time these NPs radiolabeled using a PET radioisotope. The present results validate the versatility of these nanosystems to integrate different radiometals for SPECT or PET imaging studies. Albeit these results are a proof-of-concept, further

investigations need to be addressed to understand the exact mechanisms related to the absorption, distribution, metabolism and excretion studies that are required to evaluate the real potentiality of these NPs as nuclear imaging probes.
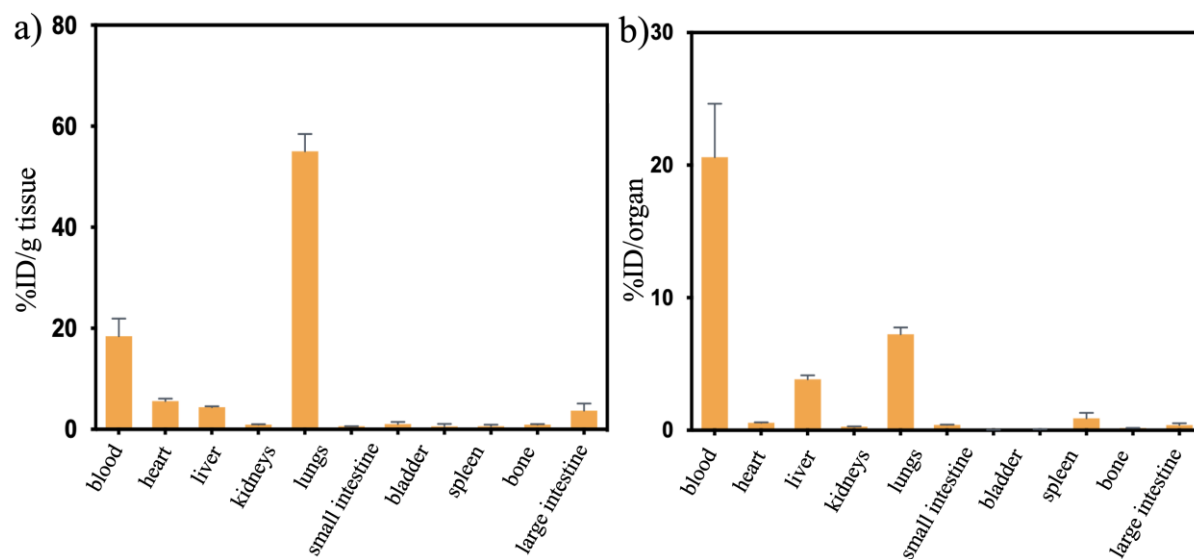
Figure 9. Quantitative biodistribution of **Cu-MPN-PEG** 5 h after i.v. injection expressed as (a) % ID/g tissue, and (b) %ID/organ. Data is presented as mean ± SD (n=3).

4. CONCLUSIONS

Indium- and copper-based MPNs with uniform sizes of 70-80 nm have been successfully synthesized via a one-pot method using catechol and bis-imidazole ligands. The MPNs can be labeled *in situ* with ^{111}In and ^{64}Cu with excellent yields feasible for *in vivo* PET/SPECT/CT imaging by simply adding a small aliquot of radionuclides into the synthesis process. Afterward, the NPs have been coated with a PDA-like polymer and subsequently functionalized with PEG ligands, reaching a final size of around 120 nm. The use of this bioinspired coating has been shown to i) improve the chemical and colloidal stability, ii) fine-tune the biodegradation of the NPs, iii) endow the NPs with a functionalizable platform and iv) reduce safety concerns. On top of that, surface modification with active targeting moieties was performed by grafting FA in the most outer surface of the NPs. Increased *in vivo* accumulation in tumors observed for **In-MPN-FA** compared to the non-functionalized MPNs, suggested that tumor-targeting could be improved by fine-tuning the NPs surface.

All these results have allowed us to demonstrate the synergism in the use of polyphenols for the formation of hybrid systems, combined NPs and coatings, which can be designed and modulated flexibly for their efficient use in PET/SPECT/CT imaging. The results presented in this manuscript for both types of MPNs are a proof-of-concept for the potential use of these NPs in molecular imaging. However, further investigation of these NPs is undergoing to understand the exact

mechanisms related to the absorption, distribution, metabolism and excretion (ADME), which is essential to optimize these NPs as probes for PET/SPECT imaging agents.

ASSOCIATED CONTENT

Supporting Information. The Supporting Information is available free of charge. Characterization of **In-MPN**, **In-MPN-PEG** and **In-MPN-FA** (Figures S1-S11 and Tables S1-S7) and **Cu-MPN**, **Cu-MPN-PEG** and **Cu-MPN-FA** (Figures S12-S24 and Tables S8-S15). Physicochemical characterization (DLS, PXRD, EDX, XPS, ^{1}H-NMR, EA and ICP-MS). Chemical stability (DLS, dialysis). Radiochemical yield calculations. *In vitro* cell uptake. Post-mortem quantification. *In vivo* SPECT/PET/CT.

AUTHOR INFORMATION

Corresponding Author

*(D.R-M.), Phone: +(34) 93733614; e-mail: dani.ruiz@icn2.cat
*(C.R.-R.), Phone: +(01) 604.827.1833; e-mail: cristina.rodriguez@ubc.ca
*(F.N), Phone: +(34) 937372648; e-mail: fernando.novio@icn2.cat

Author Contributions

The manuscript was written through the contributions of all authors. All authors have given approval to the final version of the manuscript.

Notes

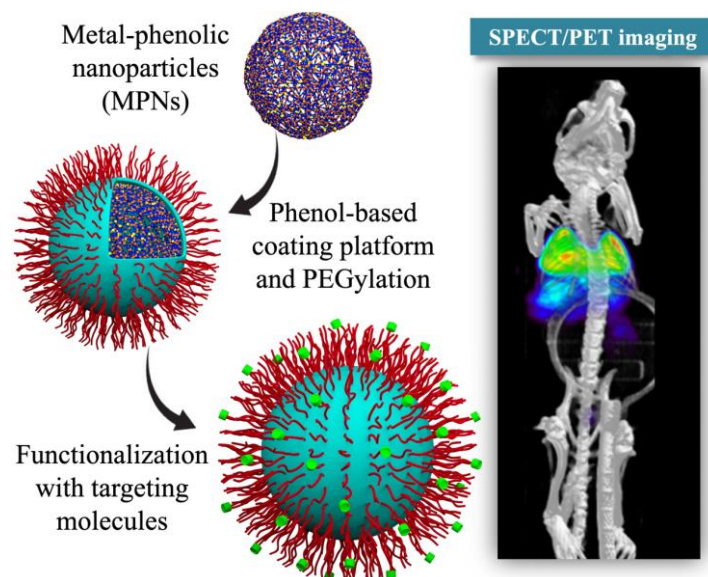The authors declare no competing financial interest.

Table of Contents

REFERENCES

[1] Rahim, M.A.; Kristufek, S.L.; Pan, S.; Richardson, J.J.; Caruso, F. Phenolic Building Blocks for the Assembly of Functional Materials. *Angew. Chem. Int. Ed. Engl.* **2019,** *58* (7), 1904-1927, DOI: 10.1002/anie.201807804.

[2] Sedó, J.; Saiz-Poseu, J.; Busqué, F.; Ruiz-Molina, D. Catechol-Based Biomimetic Functional Materials. *Adv. Mater.* **2013**, *25*, 653–701, DOI: 10.1002/9783527675821.ch11.

[3] Ryu, J.H.; Messersmith, P.B.; Lee, H. Polydopamine Surface Chemistry: A Decade of Discovery. *ACS Appl. Mater. Interfaces* **2018,** *10* (9), 7523-7540, DOI: 10.1021/acsami.7b19865.

[4] Hu, F.; Liu, B.; Chu, H.; Liu, C.; Li, Z.; Chen, D.; Li, L. Real-Time Monitoring of pH-Responsive Drug Release Using a Metal-Phenolic Network-Functionalized Upconversion Nanoconstruct. *Nanoscale* **2019,** *11* (18), 9201-9206, DOI: 10.1039/c9nr01892a.

[5] Yun, G.; Pan, S.; Wang, T.Y.; Guo, J.; Richardson, J.J.; Caruso, F. Synthesis of Metal Nanoparticles in Metal-Phenolic Networks: Catalytic and Antimicrobial Applications of Coated Textiles. *Adv Healthc. Mater.* **2018,** *7* (5), 1700934, DOI: 10.1002/adhm.201700934.

[6] Zhang, W.; Besford, Q.A.; Christofferson, A.J.; Charchar, P.; Richardson, J.J.; Elbourne, A.; Kempe, K.; Hagemeyer, C.E.; Field, M.R.; McConville, C.F.; Yarovsky, I.; Caruso, F. Cobalt-Directed Assembly of Antibodies onto Metal-Phenolic Networks for Enhanced Particle Targeting. *Nano Lett.* **2020,** *20* (4), 2660-2666, DOI: 10.1021/acs.nanolett.0c00295.

[7] Nador, F.; Novio, F.; Ruiz-Molina, D. Coordination Polymer Particles with Ligand-Centred pH-Responses and Spin Transition. *Chem. Commun.* **2014,** *50* (93), 14570-15472, DOI: 10.1039/c4cc05299d.

[8] Nador, F.; Wnuk, K.; Roscini, C.; Solórzano, R.; Faraudo, J.; Ruiz-Molina, D.; Novio, F. Solvent-Tuned Supramolecular Assembly of Fluorescent Catechol/Pyrene Amphiphilic Molecules. *Chem. Eur. J.* **2018,** *24* (55), 14724-14732, DOI: 10.1002/chem.201802249.

[9] Solórzano, R.; Tort, O.; Garcia-Pardo, J.; Escriba, T.; Lorenzo, J.; Arnedo, M.; Ruiz-Molina, D.; Alibes, R.; Busqué, F.; Novio, F. Versatile Iron-Catechol-Based Nanoscale Coordination Polymers with Antiretroviral Ligand Functionalization and their Use as Efficient Carriers in HIV/AIDS Therapy. *Biomater. Sci.* **2018,** *7* (1), 178-186, DOI: 10.1039/c8bm01221k.

[10] Zhou, J.; Lin, Z. ; Ju, Y. ; Rahim, M.D.; Richardson, J. J.; Caruso, F. Polyphenol-Mediated Assembly for Particle Engineering. *Acc. Chem. Res.* **2020**, *53*, 1269–1278, DOI: 10.1021/acs.accounts.0c00150.

[11] Zhang, X. Parekh, G.; Guo, B.; Huang, X.; Dong, Y.; Han, W.; Chen, X.; Xiao, G. Polyphenol and Self-Assembly: Metal Polyphenol Nanonetwork for Drug Delivery and Pharmaceutical Applications. *Future Drug. Discov.* **2019**, *1*(1), FDD7, DOI: 10.4155/fdd-2019-0001.

[12] Liang, H.; Zhou, B.; Wu, D.; Li, J.; Li, B. Supramolecular Design and Applications of Polyphenol-Based Architecture: A review. *Adv. Colloid Interface Sci.* **2019**, *272*, 102019, DOI: 10.1016/j.cis.2019.102019.

[13] Andersen, A.; Chen, Y.; Birkedal, H. Bioinspired Metal–Polyphenol Materials: Self-Healing and Beyond. *Biomimetics* **2019**, *4*, 30, DOI: 10.3390/biomimetics4020030.

[14] Ejima, H.; Richardson, J. J.; Caruso, F. Metal-phenolic Networks as a Versatile Patform to Engineer Nanomaterials and Biointerfaces. *Nano Today* **2017,** *12*, 136-148, DOI: 10.1016/j.nantod.2016.12.012.

[15] Guo, J.; Ping, Y.; Ejima, H.; Alt, K.; Meissner, M.; Richardson, J.J.; Yan, Y.; Peter, K.; von Elverfeldt, D.; Hagemeyer, C.E.; Caruso, F. Engineering Multifunctional Capsules through the Assembly of Metal-Phenolic Networks. *Angew. Chem. Int. Ed. Engl.* **2014,** *53* (22), 5546-5551, DOI: 10.1002/anie.201311136.

[16] Wang, H.: Wang, C.; Zou, Y.; Hu, J.; Li, Y.; Cheng, Y. Natural Polyphenols in Drug Delivery Systems: Current Status and Future Challenges. *Giant* **2020**, *3*, 100022, DOI:10.1016/j.giant.2020.100022.

[17] Suárez-García, S.; Arias-Ramos, N.; Frias, C.; Candiota, A. P.; Arus, C.; Lorenzo, J.; Ruiz-Molina, D.; Novio, F. Dual T1/ T2 Nanoscale Coordination Polymers as Novel Contrast Agents for MRI: A Preclinical Study for Brain Tumor. *ACS Appl. Mater. Interfaces* **2018,** *10*, 38819-38832, DOI: 10.1021/acsami.8b15594.

[18] Borges, M.; Yu, S.; Laromaine, A.; Roig, A.; Suárez-García, S.; Lorenzo, J.; Ruiz-Molina, D.; Novio, F. Dual T1/T2 MRI Contrast Agent Based on Hybrid SPION@Coordination Polymer Nanoparticles. *RSC Advances* **2015**, *5*, 86779-86783, DOI: 10.1039/C5RA17661A.

[19] Qin, J.; Liang, G.; Feng, Y.; Feng, B.; Wang, G.; Wu, N.; Zhao, Y.; Wei, J. Synthesis of Gadolinium/Iron–Bimetal–Phenolic Coordination Polymer Nanoparticles for Theranostic Applications. *Nanoscale* **2020**, *12*, 6096–6103, DOI: 10.1039/C9NR10020B.

[20]Shin, M.; Park, E.; Lee, H. Plant-Inspired Pyrogallol-Containing Functional Materials. *Adv. Funct. Mater.* **2019**, *29*, 1903022, DOI: 10.1002/adfm.201903022.

[21] Dai, Q.; Geng, H.; Yu, Q.; Hao, J.; Cui, J. Polyphenol-Based Particles for Theranostics. *Theranostics* **2019**, 9(11), 3170-3190, DOI: 10.7150/thno.31847.

[22] Wang, X.; Yan, J.; Pan, D.; Yang, R.; Wang, L.; Xu, Y.; Sheng, J.; Yue, Y.; Huang, Q.; Wang, Y.; Wang, R.; Yang, M. Polyphenol-Poloxamer Self-Assembled Supramolecular Nanoparticles for Tumor NIRF/PET Imaging. *Adv. Healthc. Mater.* **2018,** *7* (15), e1701505, DOI: 10.1002/adhm.201701505.

[23] Shana, L.; Gao, W.; Wang, W.; Tang, W.; Wang, Z.; Yang, Z.; Fan, W.; Zhu, G.; Zhai, K.; Jacobson, O.; Daic, Y.; Chen, X. Self-Assembled Green Tea Polyphenol-Based Coordination Nanomaterials to Improve Chemotherapy Efficacy by Inhibition of Carbonyl Reductase 1. *Biomaterials* **2019**, *210*, 62–69, DOI: 10.1016/j.biomaterials.2019.04.032.

[24] Dai, Y.; Cheng, S.; Wang, Z.; Zhang, R.; Yang, Z.; Wang, J.; Yung, B. C.; Wang, Z.; Jacobson, O.; Xu, C.; Ni, Q.; Yu, G.; Zhou, Z.; Chen, X. Hypochlorous Acid Promoted Platinum Drug Chemotherapy by Myeloperoxidase-Encapsulated Therapeutic Metal Phenolic Nanoparticles. *ACS Nano* **2018**, *12*, 455-463, DOI: 10.1021/acsnano.7b06852.

[25] Yang, Z.; Dai, Y.; Shan, L.; Shen, Z.; Wang, Z. Yung, B. C.; Jacobson, O.; Liu, Y.; Tang, W.; Wang, S.; Lin, L.; Niu, G.; Huang, P.; Chen, X. Tumour Microenvironment-Responsive Semiconducting Polymer-based Self-Assembling Nanotheranostics. *Nanoscale Horiz.* **2019**, *4*, 426-433, DOI: 10.1039/C8NH00307F.

[26] Jin, Q.; Zhu, W.; Jiang, D.; Zhang, R.; Kutyreff, C. J.; Engle, J. W.; Huang, P.; Cai, W.; Liu, Z.; Cheng, L. Ultra-Small Iron-Gallic Acid Coordination Polymer Nanoparticles for Chelator-Free Labeling of (64)Cu and Multimodal Imaging-Guided Photothermal Therapy. *Nanoscale* **2017**, *9*, 12609-12617, DOI: 10.1039/c7nr03086j.

[27] Shen, S.; Jiang, D.; Cheng, L.; Chao, Y.; Nie, K.; Dong, Z.; Kutyreff, C.J.; Engle, J.W.; Huang, P.; Cai, W.; Liu, Z. Renal-Clearable Ultrasmall Coordination Polymer Nanodots for Chelator-Free ^{64}Cu-Labeling and Imaging-Guided Enhanced Radiotherapy of Cancer. *ACS Nano* **2017**, *11*, 9103-9111, DOI: 10.1021/acsnano.7b03857.

[28] Liu, Y.; Ai, K.; Lu, L. Polydopamine and its Derivative Materials: Synthesis and Promising Applications in Energy, Environmental, and Biomedical Fields. *Chem. Rev.* **2014,** *114*, 5057-5115, DOI: 10.1021/cr400407a.

[29] Lynge, M.E.; van der Westen, R.; Postma, A.; Stadler, B. Polydopamine-A Nature-Inspired Polymer Coating for Biomedical Science. *Nanoscale* **2011,** *3* (12), 4916-4928, DOI: 10.1039/c1nr10969c.

[30] Ding, Y.H.; Floren, M.; Tan, W. Mussel-Inspired Polydopamine for Bio-Surface Functionalization. *Biosurf. Biotribol.* **2016,** *2* (4), 121-136, DOI: 10.1016/j.bsbt.2016.11.001.

[31] Kang, S. M.; Rho, J.; Choi, I. S.; Messersmith, P.B.; Lee, H. Norepinephrine: Material-Independent, Multifunctional Surface Modification Reagent. *J. Am. Chem. Soc.* **2009,** *131* (37), 13224-13225, DOI: 10.1021/ja905183k.

[32] Kuang, J.; Guo, J.L.; Messersmith, P.B. High Ionic Strength Formation of DOPA-Melanin Coating for Loading and Release of Cationic Antimicrobial Compounds. *Adv. Mater. Interfaces* **2014,** *1* (6), 1400145, DOI: 10.1002/admi.201400145.

[33] Lim, C.; Huang, J.; Kim, S.; Lee, H.; Zeng, H.; Hwang, D. S. Nanomechanics of Poly(catecholamine) Coatings in Aqueous Solutions. *Angew. Chem. Int. Ed. Engl.* **2016,** *55* (10), 3342-3346, DOI: 10.1002/anie.201510319.

[34] Saiz-Poseu, J.; Mancebo-Aracil, J.; Nador, F.; Busque, F.; Ruiz-Molina, D. The Chemistry behind Catechol-Based Adhesion. *Angew. Chem. Int. Ed. Engl.* **2019,** *58* (3), 696-714, DOI: 10.1002/anie.201801063.

[35] Hong, S.; Na, Y.S.; Choi, S.; Song, I.T.; Kim, W.Y.; Lee, H. Non- Covalent Self- Assembly and Covalent Polymerization Co- Contribute to Polydopamine Formation. *Adv. Funct. Mater.* **2012,** *22*, 4711-4717, DOI: 10.1002/adfm.201201156.

[36] Cai, Z.; Shi, J.; Li, W.; Wu, Y.; Zhang, Y.; Zhang, S.; Jiang, Z. Mussel-Inspired pH-Switched Assembly of Capsules with an Ultrathin and Robust Nanoshell. *ACS Appl. Mater. Interfaces* **2019,** *11* (31), 28228-28235, DOI: 10.1021/acsami.9b11445.

[37] Nador, F.; Guisasola, E.; Baeza, A.; Villaecija, M.A.; Vallet-Regi, M.; Ruiz-Molina, D. Synthesis of Polydopamine-Like Nanocapsules via Removal of a Sacrificial Mesoporous Silica Template with Water. *Chemistry* **2017,** *23* (12), 2753-2758, DOI: 10.1002/chem.201604631.

[38] Wang, Y.; Shang, B.; Liu, M.; Shi, F.; Peng, B.; Deng, Z. Hollow Polydopamine Colloidal Composite Particles: Structure Tuning, Functionalization and Applications. *J. Colloid Interface Sci.* **2018,** *513*, 43-52, DOI: 10.1016/j.jcis.2017.10.102.

[39] Saiz-Poseu, J.; Sedó, J.; Garcia, B.; Benaiges, C.; Parella, T.; Alibes, R.; Hernando, J.; Busqué, F.; Ruiz-Molina, D. Versatile Nanostructured Materials via Direct Reaction of Functionalized Catechols. *Adv. Mater.* **2013,** *25* (14), 2066-2070, DOI: 10.1002/adma.201204383.

[40] Lee, H.; Dellatore, S.M.; Miller, W.M.; Messersmith, P.B. Mussel-Inspired Surface Chemistry for Multifunctional Coatings. *Science* **2007,** *318* (5849), 426-430, DOI: 10.1126/science.1147241.

[41] Liu, X.; Cao, J.; Li, H.; Li, J.; Jin, Q.; Ren, K.; Ji, J. Mussel-Inspired Polydopamine: A Biocompatible and Ultrastable Coating for Nanoparticles in Vivo. *ACS Nano* **2013,** *7* (10), 9384-9395, DOI: 10.1021/nn404117j.

[42] Ambekar, R. S.; Kandasubramanian, B. A Polydopamine-Based Platform for Anti-Cancer Drug Delivery. *Biomater. Sci.* **2019,** *7* (5), 1776-1793, DOI: 10.1039/c8bm01642a.

[43] Ambekar, R. S.; Kandasubramanian, B. A Polydopamine-Based Platform for Anti-Cancer Drug Delivery. *Biomater. Sci.* **2019,** *7* (5), 1776-1793, DOI: 10.1039/c8bm01642a.

[44] Cheng, W.; Nie, J.; Gao, N.; Liu, G.; Tao, W.; Xiao, X.; Jiang, L.; Liu, Z.; Zeng, X.; Mei, L. A Multifunctional Nanoplatform Against Multidrug Resistant Cancer: Merging the Best of Targeted Chemo/Gene/Photothermal Therapy. *Adv. Funct.Mater.* **2017,** *27* (45), 1704135, DOI: 10.1002/adfm.201704135.

[45] Lin, X.; Cao, Y.; Li, J.; Zheng, D.; Lan, S.; Xue, Y.; Yu, F.; Wu, M.; Zhu, X. Folic Acid-Modified Prussian Blue/Polydopamine Nanoparticles as an MRI Agent for Use in Targeted Chemo/Photothermal Therapy. *Biomater. Sci.* **2019,** *7* (7), 2996-3006, DOI: 10.1039/c9bm00276f.

[46] Dai, Y.; Yang, Z.; Cheng, S.; Wang, Z.; Zhang, R.; Zhu, G.; Wang, Z.; Yung, B. C.; Tian, R.; Jacobson, O.; Xu, C.; Ni, Q.; Song, J.; Sun, X.; Niu, G.; Chen, X. Toxic Reactive Oxygen Species Enhanced Synergistic Combination Therapy by Self-Assembled Metal-Phenolic Network Nanoparticles. *Adv. Mater.* **2018,** *30* (8), 1704877, DOI: 10.1002/adma.201704877.

[47] Novio, F.; Lorenzo, J.; Nador, F.; Wnuk, K.; Ruiz-Molina, D. Carboxyl Group (-CO$_2$H) Functionalized Coordination Polymer Nanoparticles as Efficient Platforms for Drug Delivery. *Chemistry* **2014,** *20* (47), 15443-15450, DOI: 10.1002/chem.201403441.

[48] Suárez-García, S.; Sedó, J.; Saiz-Poseu, J.; Ruiz-Molina, D. Copolymerization of a Catechol and a Diamine as a Versatile Polydopamine-Like Platform for Surface Functionalization: The Case of a Hydrophobic Coating. *Biomimetics* **2017,** *2* (4), 22. DOI: 10.3390/biomimetics2040022.

[49] Lyu, Q.; Zhang, J.; Neoh, K.G.; Chai, C.L.L. A One Step Method for the Functional and Property Modification of DOPA Based Nanocoatings. *Nanoscale* **2017,** *9* (34), 12409-12415, DOI: 10.1039/c7nr05293f.

[50] Iacomino, M.; Paez, J.I.; Avolio, R.; Carpentieri, A.; Panzella, L.; Falco, G.; Pizzo, E.; Errico, M.E.; Napolitano, A.; Del Campo, A.; d'Ischia, M. Multifunctional Thin Films and Coatings from Caffeic Acid and a Cross-Linking Diamine. *Langmuir* **2017,** *33* (9), 2096-2102, DOI: 10.1021/acs.langmuir.6b04079.

[51] Yang, Y.; Qi, P.; Ding, Y.; Maitz, M.F.; Yang, Z.; Tu, Q.; Xiong, K.; Leng, Y.; Huang, N. A Biocompatible and Functional Adhesive Amine-Rich Coating Based on Dopamine Polymerization. *J. Mater. Chem. B* **2015,** *3* (1), 72-81, DOI: 10.1039/c4tb01236d.

[52] Chen, S.; Li, X.; Yang, Z.; Zhou, S.; Luo, R.; Maitz, M. F.; Zhao, Y.; Wang, J.; Xiong, K.; Huang, N. A Simple One-Step Modification of Various Materials for Introducing Effective Multifunctional Groups. *Colloids Surf. B Biointerfaces* **2014,** *113*, 125-133, DOI: 10.1016/j.colsurfb.2013.08.041.

[53] Alfieri, M.L.; Panzella, L.; Oscurato, S.L.; Salvatore, M.; Avolio, R.; Errico, M.E.; Maddalena, P.; Napolitano, A.; Ball, V.; d'Ischia, M. Hexamethylenediamine-Mediated Polydopamine Film Deposition: Inhibition by Resorcinol as a Strategy for Mapping Quinone Targeting Mechanisms. *Front. Chem.* **2019,** *7*, 407, DOI: 10.3389/fchem.2019.00407.

[54] Adarsh, N.N.; Novio, F.; Ruiz-Molina, D. Coordination Polymers Built from 1,4-bis(imidazol-1-ylmethyl)benzene: From Crystalline to Amorphous. *Dalton Trans.* **2016,** *45* (28), 11233-11255, DOI: 10.1039/c6dt01157h.

[55] Goorden, M.C.; van der Have, F.; Kreuger, R.; Ramakers, R.M.; Vastenhouw, B.; Burbach, J.P.; Booij, J.; Molthoff, C.F.; Beekman, F. J. VECTor: A Preclinical Imaging System for Simultaneous Submillimeter SPECT and PET. *J. Nucl. Med.* **2013,** *54* (2), 306-312, DOI: 10.2967/jnumed.112.109538.

[56] Branderhorst, W.; Vastenhouw, B.; Beekman, F.J. Pixel-Based Subsets for Rapid Multi-Pinhole SPECT Reconstruction. *Phys. Med. Biol.* **2010,** *55* (7), 2023-2034, DOI: 10.1088/0031-9155/55/7/015.

[57] Foster, H.L.; Small, J.D.; Fox, J.G. *The mouse in biomedical research.* **1983**, New York: Academic Press.

[58] Amorin-Ferre, L.; Busqué, F.; Bourdelande, J.L.; Ruiz-Molina, D.; Hernando, J.; Novio, F. Encapsulation and Release Mechanisms in Coordination Polymer Nanoparticles. *Chemistry* **2013,** *19* (51), 17508-17516, DOI: 10.1002/chem.201302662.

[59] Stockhofe, K.; Postema, J. M.; Schieferstein, H.; Ross, T. L. Radiolabeling of Nanoparticles and Polymers for PET Imaging. *Pharmaceuticals* **2014,** *7* (4), 392-418, DOI: 10.3390/ph7040392.

[60] Benns, J. M.; Maheshwari, A.; Furgeson, D. Y.; Mahato, R. I.; Kim, S. W. Folate-PEG-Folate-Graft-Polyethylenimine-Based Gene Delivery. *J. Drug Target* **2001,** *9* (2), 123-139, DOI: 10.3109/10611860108997923.

[61] Agnoletti, M.; Rodriguez-Rodriguez, C.; Klodzinska, S.N.; Esposito, T.V.F.; Saatchi, K.; Moerk, N.H.; Häfeli, U.O. Monosized Polymeric Microspheres Designed for Passive Lung Targeting: Biodistribution and Pharmacokinetics after Intravenous Administration. *ACS Nano* **2020**, *14*, 6693-6706. DOI: 10.1021/acsnano.9b09773.

[62] Braakhuis, H.M.; Park, M.; Gosens, I.; De Jong, W.H.; Cassee, F.R. Physicochemical Characteristics of Nanomaterials that Affect Pulmonary Inflammation. *Part. Fibre Toxicol.* **2014**, *11*, 18. DOI: 10.1186/1743-8977-11-18.

[63] Townsley, M. I., Structure and Composition of Pulmonary Arteries, Capillaries, and Veins. *Compr. Physiol.* 2012, *2* (1), 675-709. DOI: 10.1002/cphy.c100081.

[64] Häfeli, U. O.; Saatchi, K.; Elischer, P.; Misri, R.; Bokharaei, M.; Labiris, N. R.; Stoeber, B., Lung Perfusion Imaging with Monosized Biodegradable Microspheres. *Biomacromolecules* 2010, *11* (3), 561-7. DOI: 10.1021/bm9010722.

[65] Kohane, D. S., Microparticles and Nanoparticles for Drug Delivery. *Biotechnol. Bioeng.* 2007, *96* (2), 203-9. DOI: 10.1002/bit.21301.

[66] Bajc, M.; Neilly, J. B.; Miniati, M.; Schuemichen, C.; Meignan, M.; Jonson, B., EANM Guidelines for Ventilation/Perfusion Scintigraphy : Part 1. Pulmonary Imaging with Ventilation/Perfusion Single Photon Emission Tomography. *Eur. J. Nucl. Med. Mol. Imaging* 2009, *36* (8), 1356-70. DOI: 10.1007/s00259-009-1170-5.

[67] Zhang, Y.-N.; Poon, W.; Tavares, A.J.; McGilvray, I.D.; Chan, W.C.W. Nanoparticle-Liver Interactions: Cellular Uptake and Hepatobiliary Elimination. *J. Control. Release* **2016**, *240*, 332-348. DOI: 10.1016 / j.jconrel.2016.01.020.

[68] Ernsting, M. J.; Murakami, M.; Roy, A.; Li, S.-D. Factors Controlling the Pharmacokinetics, Biodistribution and Intratumoral Penetration of Nanoparticles. *J. Control Release* **2013**, *172*, 782-794, DOI: 10.1016/j.jconrel.2013.09.013